

**Kerr measurements of electron
polarization**

INAUGURAL-DISSERTATION

zur
Erlangung der Würde eines Doktors der Philosophie,
vorgelegt der Philosophisch-Naturwissenschaftlichen Fakultät
der Universität Basel

von

STEPHAN ROBINSON

aus Küsnacht ZH

Basel 1994

Genehmigt von der Philosophisch-Naturwissenschaftlichen Fakultät

auf Antrag der

Herren Professoren Dr. I. Sick und Dr. P. Oelhafen.

Basel, den 1. März 1994

Prof. Dr. H. Rowell

Dekan

Acknowledgments

I want to express at this place my gratitude to Prof. Dr. I. Sick for his teaching me the essence of being a physicist.

I am also thankful to Drs. L.J. de Bever and A. Feltham and to M. Loppacher for their continuing interest and their critics in the development of the Kerr apparatus. To P. Schmid for his support in computer matters and M. Steinacher for his aid in questions of electronics. And to all my colleagues for our shared time.

Finally I want to thank my grandparents, my mother, Ru and Nana for their support in these not always easy times.

Contents

1	Introduction	1
2	Møller scattering	2
2.1	Theory of Møller scattering	2
2.1.1	General formulation	2
2.1.2	Formulation for electron energies above 1 GeV	3
2.2	Lay-out of a double arm Møller polarimeter	4
2.3	Extraction of the beam polarization	5
2.3.1	Møller count rate	5
2.3.2	Calculation of beam polarization	6
2.4	Background channels	6
2.5	Intra-atomic motion of bound electrons	8
3	Møller target	9
3.1	In-plane polarization	9
3.1.1	Set up of the target	9
3.1.2	Extraction of target polarization	10
3.2	Out-of-plane polarization	11
3.2.1	Set up of the target	11
3.2.2	Magnetic saturation of the target	12
3.2.3	Advantages of concept	12
3.2.4	Possible target materials	12

CONTENTS

4	The Kerr apparatus	14
4.1	The Kerr effect	14
4.2	Set up	17
4.3	Description of individual components	17
4.4	Hints and clues	21
5	Measurements	25
5.1	Temporal stability	25
5.2	Temperature effects	27
5.3	Kerr measurement	30
5.4	Target rotation	30
6	Practical details	32
6.1	Measurement procedure	32
6.2	Target surface	32
6.3	Multiple scattering in the target	33
6.4	Power deposition in the target	33
6.4.1	Heating up of a round stationary target	34
6.4.2	Heating up of a round rotating target	34
6.4.3	Heating up of a moving ribbon target	35
6.4.4	Radiation cooling	36
6.5	Eddy currents in a rotating target	36
6.6	Transversal polarization components	37
6.6.1	Longitudinally polarized target	37
6.6.2	Transversally polarized target	38
6.6.3	Measuring time	39
7	Conclusions	40
A	Calculating optical properties with help of the Jones matrix calculus	41
A.1	Phasor notation	41
A.2	Matrix representation of polarized light	42

A.2.1	Linear and circular polarization	42
A.2.2	Elliptic polarization	43
A.3	Calculations of this optical set up	43
A.3.1	List of optical matrices employed	43
A.3.2	Diode response of an ideal optical system	44
A.3.3	Diode response of a non-ideal optical system	46
B	About magnetism	50
B.1	Free magnetic moments in ferromagnets	50
B.2	The factors g and g'	51
B.3	Magnetization and temperature	54
B.4	Iron polarization at room temperature	54
B.5	Conversion table of magnetic quantities	55
B.6	Magnetic relationships in matter	55
C	Theoretical explanation of the Kerr effect	56
C.1	Macroscopic description	56
C.2	Microscopic description	59
D	Suppliers	61
	Bibliography	62

Chapter 1

Introduction

In investigations of the properties of atomic nuclei accelerated particles are used as probes. Various types of information can be extracted by employing different classes of probes like leptons or hadrons. The use of spin polarized targets and/or beams opens a new class of very precise and fundamental experiments but it requires the ability to measure spin polarization.

Measuring the spin polarization of a beam is done by scattering the accelerated particles off a thin foil of appropriate material. One or several detectors measure the count rate of the scattered particles. Generally this count rate has a left-right, up-down or parallel-antiparallel asymmetry, depending on the orientation of the beam spins. As this asymmetry is linearly dependent on beam polarization, this allows to extract the desired information.

In low energy electron experiments the beam polarization is measured with help of Mott scattering. In the range of MeV- and GeV-energies this method is no longer appropriate. In 1975 the first polarization measurement in the GeV-region was performed by P.S. Cooper. To this aim he used polarized Møller-scattering ($\vec{e} - \vec{e}$) in a single arm experiment [Co75]. The method was improved ten years later by B. Wagner. By introducing a quadrupole magnet after the target he could measure the two Møller electrons in coincidence [Wa86]. This method largely reduces the background hereby increasing the precision of polarization measurements.

Nowadays the main uncertainty in determining the beam polarization arises from an insufficient knowledge of target polarization, which is known to about 3 %. This work describes a new concept which will allow an online measurement of target polarization with an error of less than 1 %.

Chapter 2

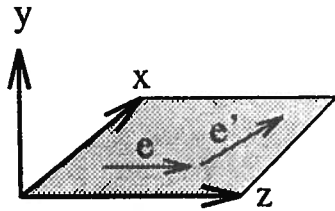
Møller scattering

This chapter presents first the theory of Møller scattering. Then the basic lay-out of a Møller polarimeter is presented. Different aspects as kinematics, extraction of the beam polarization and background processes are discussed.

2.1 Theory of Møller scattering

2.1.1 General formulation

The coordinate system used is defined in terms of the momentum of the incident and scattered electron:



$$\vec{e}_z = \frac{\vec{k}}{|\vec{k}|} ; \vec{e}_y = \frac{\vec{k} \times \vec{k}'}{|\vec{k} \times \vec{k}'|} ; \vec{e}_x = \vec{e}_y \times \vec{e}_z \quad (2.1)$$

where \vec{k} and \vec{k}' represent the momenta of the incident and scattered electrons. The Møller cross section per electron can be written as¹:

$$\frac{d\sigma}{d\Omega} = \frac{d\sigma^0}{d\Omega} \left(1 + \sum_{i,j} A_{ij} \cdot P_i^B \cdot P_j^T \right) \quad \text{with } i, j = x, y, z, \quad (2.2)$$

where P^B and P^T are beam and target polarization respectively, $\frac{d\sigma^0}{d\Omega}$ the cross section for unpolarized electrons and A_{ij} the asymmetry coefficients. The latter can be calculated exactly from QED. Using the notation of [Wa86]² we can express them as:

¹Center of mass (CM) values are overlined throughout.

²see also [Ol68, Fo57]

$$\frac{d\sigma^o}{d\Omega} = \left(\frac{r_o}{2 \cdot \bar{\gamma} \cdot (\bar{\gamma}^2 - 1) \cdot \sin^2 \bar{\theta}} \right)^2 \cdot a_o \cdot \frac{1}{100} \quad (2.3)$$

$$A_{xx} = -\sin^2 \bar{\theta} \cdot \left((2\bar{\gamma}^2 - 1) + (\bar{\gamma}^4 - 1) \cdot \sin^2 \bar{\theta} \right) / a_o \quad (2.4)$$

$$A_{yy} = -\sin^2 \bar{\theta} \cdot \left((4\bar{\gamma}^2 - 3) - (\bar{\gamma}^2 - 1)^2 \cdot \sin^2 \bar{\theta} \right) / a_o \quad (2.5)$$

$$A_{zz} = -\sin^2 \bar{\theta} \cdot \left((2\bar{\gamma}^2 - 1) \cdot (4\bar{\gamma}^2 - 3) - (\bar{\gamma}^4 - 1) \cdot \sin^2 \bar{\theta} \right) / a_o \quad (2.6)$$

$$A_{xz} = A_{zx} = +2 \cdot \sin^2 \bar{\theta} \cdot \bar{\gamma} \cdot (\bar{\gamma}^2 - 1) \cdot \sin \bar{\theta} \cdot \cos \bar{\theta} / a_o \quad (2.7)$$

$$A_{xy} = A_{yx} = A_{yz} = A_{zy} = 0, \quad (2.8)$$

with $\bar{\gamma} = \sqrt{(E_o + m_e)/2m_e}$
 E_o = kinetic energy of the incident electron in MeV
 m_e = 0.511 = rest mass of the electron in MeV
 $\bar{\theta}$ = scattering angle of the Møller electron
 $a_o = (2\bar{\gamma}^2 - 1)^2 \cdot (4 - 3\sin^2 \bar{\theta}) + (\bar{\gamma}^2 - 1)^2 \cdot (4 + \sin^2 \bar{\theta}) \cdot \sin^2 \bar{\theta}$
 $r_o = 2.818$ = electron radius in fm
 $\frac{1}{100}$ = conversion factor from fm² to barn

2.1.2 Formulation for electron energies above 1 GeV

At high energies (≥ 1 GeV) the expressions given above simplify and become energy-independent (with the exception of the differential cross section):

$$\frac{d\sigma^o}{d\Omega} \rightarrow \left(\frac{r_o}{2 \cdot \bar{\gamma}} \cdot \frac{4 - \sin^2 \bar{\theta}}{\sin^2 \bar{\theta}} \right)^2 \quad (2.9)$$

$$A_{xx} \rightarrow -\frac{\sin^4 \bar{\theta}}{(4 - \sin^2 \bar{\theta})^2} \quad (2.10)$$

$$A_{yy} \rightarrow -A_{xx} \quad (2.11)$$

$$A_{zz} \rightarrow -\frac{\sin^2 \bar{\theta} \cdot (8 - \sin^2 \bar{\theta})}{(4 - \sin^2 \bar{\theta})^2} \quad (2.12)$$

$$A_{xz} \rightarrow 0 \quad (2.13)$$

The kinematics of the normally used 90° CM Møller polarimeter can now be derived from equations (2.9) – (2.13):

Møller scattering observed at an angle $\bar{\theta} = 90^\circ$ has following properties:

1. The asymmetry coefficients assume their maximum value:

$$A_{xx}(\bar{\theta} = 90^\circ) = -1/9 \quad (2.14)$$

$$A_{yy}(\bar{\theta} = 90^\circ) = +1/9 \quad (2.15)$$

$$A_{zz}(\bar{\theta} = 90^\circ) = -7/9 \quad (2.16)$$

As only experiments with longitudinally polarized electrons are of interest³ the Møller polarimeter must exploit A_{zz} . This consequently requires a longitudinally polarized target.

2. The lab cross section becomes a constant:

$$\frac{d\sigma^o}{d\Omega}(\bar{\theta} = 90^\circ) = 178 \frac{\text{mbarn}}{\text{sr}} \quad (2.17)$$

3. The lab scattering angle of the scattered and the recoiling electron are identical. The two electrons each carry half of the incident electron energy.

A main problem for a 90° CM set up are the small laboratory scattering angles. Typical values are:

E_{Beam} (GeV)	scattering angle (lab)
1	1.83°
3	1.06°
6	0.75°

These small angles lead to an unreasonable polarimeter length if no quadrupole or septum magnet is inserted. Magnetic deflection also opens the possibility to direct the electrons towards the detector for different electron energies simply by tuning the magnetic field strength.

2.2 Lay-out of a double arm Møller polarimeter

The term Møller scattering denotes the process of electron-electron scattering ($e - e$). If both electrons are polarized, the scattering process ($\vec{e} - \vec{e}$) can be used for polarimetry.

A target with polarized electrons is obtained by magnetizing a thin foil of ferromagnetic material. The spins of the target electrons align with the direction of the magnetic field.

³The reaction cross section of transversally polarized electrons is attenuated by a factor $\frac{1}{7}$ compared to the longitudinal reaction.

An incoming beam electron scattering off a target electron leads to two electrons leaving the target under a small angle. Increasing this angle is done by placing a quadrupole downstream of the target. The beam electrons are little affected by the quadrupole field as they go through the field free center, whereas the interacting electrons are deflected. A set of detectors identifies the two Møller electrons by a coincidence measurement.

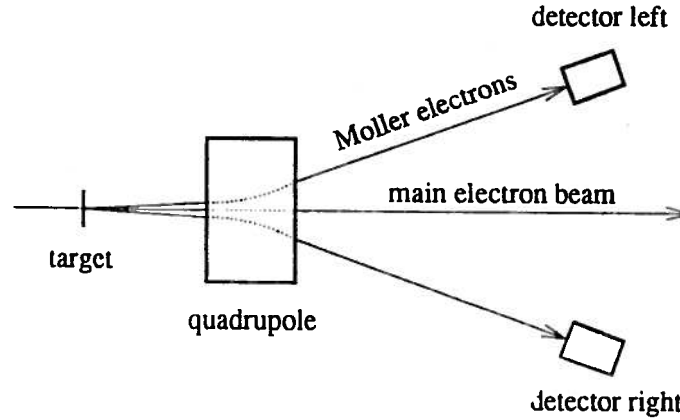


Figure 2.1: Set up of a two arm Møller polarimeter

2.3 Extraction of the beam polarization

2.3.1 Møller count rate

The general expression for count rates N is the product:

$$N = e^- \text{ in the target} \times e^- \text{ in the beam} \times \text{diff. cross section} \times \text{solid angle}$$

$$= \underbrace{\rho \left[\frac{g}{\text{cm}^3} \right] \cdot d[\text{cm}] \cdot N_{\text{Avogadro}} \left[\frac{1}{g} \right] \cdot \frac{Z}{A}}_{\text{electrons in the target}} \cdot \underbrace{N_{\text{Beam}} \left[\frac{\text{electrons}}{\text{sec}} \right]}_{\text{electrons in the beam}} \cdot \frac{d\sigma^\circ}{d\Omega} \left[\frac{\text{cm}^2}{\text{sr}} \right] \cdot d\Omega[\text{sr}] \quad (2.18)$$

$$N = L \left[\frac{\text{electrons}}{\text{cm}^2 \cdot \text{s}} \right] \cdot \frac{d\sigma^\circ}{d\Omega} \left[\frac{\text{cm}^2}{\text{sr}} \right] \cdot d\Omega[\text{sr}] \quad (2.19)$$

L is called the luminosity. This count rate does not yet include polarization effects. If beam and target are both longitudinally polarized, $\frac{d\sigma^\circ}{d\Omega}$ has to be replaced by the polarized cross section:

$$\frac{d\sigma}{d\Omega} = \frac{d\sigma^\circ}{d\Omega} \cdot (1 \pm A_{zz} P_B P_T) \quad (2.20)$$

2.3.2 Calculation of beam polarization

Knowing the (normalized) count rates for target and beam spins parallel (N^+) and antiparallel (N^-), the use of equation 2.19 leads to:

$$N^+ = L \cdot d\Omega \cdot \frac{d\sigma^o}{d\Omega} \cdot (1 + A_{zz} P_B P_T) \quad ; \quad N^- = L \cdot d\Omega \cdot \frac{d\sigma^o}{d\Omega} \cdot (1 - A_{zz} P_B P_T) \quad (2.21)$$

$$\frac{N^+ - N^-}{N^+ + N^-} = A_{zz}^{exp} = A_{zz}^{th} P_T P_B \quad (2.22)$$

With A_{zz}^{th} calculated by QED (see eq. 2.6) and P_T measured with an appropriate technique, the beam polarization can now be extracted:

$$P_B = \frac{1}{A_{zz}^{th} P_T} \frac{N^+ - N^-}{N^+ + N^-} \quad (2.23)$$

The relative error is given by quadratic addition of the statistical and the systematic errors:

$$\frac{\Delta P_B}{P_B} = \sqrt{\frac{4N^+ N^-}{(N^+ + N^-)(N^+ - N^-)^2} + \left(\frac{\Delta P_T}{P_T}\right)^2} \quad (2.24)$$

The measuring time has following functional dependence (when neglecting systematic errors):

$$T(I, P_B, \frac{\Delta P_B}{P_B}) = \frac{\text{constant}(\frac{\Delta P_B}{P_B})}{I \cdot P_B^2} \quad (2.25)$$

2.4 Background channels

The single-arm Møller polarimeter used by Cooper [Co75] (measuring electrons of energies of 6 – 19 GeV) showed a background consistent with the radiative tail of Mott scattered electrons. These electrons result from scattering off a nucleus and losing at the same time a fraction of their energy in a bremsstrahlung process. The target nuclei being unpolarized this background is spin-independent. The Mott scattered events form a smooth background behaving roughly as $d^2 N/d\theta dp \sim 1/p\theta^4$. As Møller scattering depends linearly on Z whereas Mott scattering increases with Z^2 , the background increases for heavy nuclei.

Although the above-mentioned experiment showed no sign of other background sources, the cross sections for both Mott scattering and several other possible channels have been calculated:

1. **Mott scattering off nuclei, including the radiative tail.** The differential cross section for iron was calculated with the code RADTAIL⁴ (which includes the form factor for iron). The values are:

$$\begin{aligned} E_{Beam} = 3 \text{ GeV} & \quad 2.4 \text{ mbarn}/(\text{MeV}\cdot\text{sr}) \\ E_{Beam} = 4 \text{ GeV} & \quad 1.8 \text{ mbarn}/(\text{MeV}\cdot\text{sr}) \end{aligned}$$

For the CEBAF Hall C polarimeter this gives a Mott background (integrated over the energy acceptance) of the order of 720 mbarn/sr. The Møller cross section in iron is 26×180 mbarn/sr thus the counting rate ratio Møller to Mott equals 6.5 : 1. Many of the Mott electrons can be eliminated by use of the coincidence condition. For a beam current of 100 μA and a coincidence time of 1 ns we have a ratio real to accidental of:

$$\frac{S}{N} = \frac{\text{count rate signal}}{(\text{count rate noise})^2 \cdot \text{coincidence time}} = \frac{226 \text{ MHz}}{(35 \text{ MHz})^2 \cdot 10^{-9}} = 184 \quad (2.26)$$

2. **Electron-interactions with the shell electrons.** Interactions with target electrons beyond the one-step Møller process were estimated by Monte-Carlo calculations with the EGS4 code. The code includes following reactions: bremsstrahlung, positron annihilation, Molière-scattering (a rough approximation of interactions with the nucleus), Møller- and Bhabha-scattering, continuous energy loss in matter, pair production, Compton scattering, coherent scattering and photoelectric effect. The simulation was done for iron targets of different thicknesses and at different beam energies. Electrons reaching the detector were grouped according to their reaction in the target. Only a very small background attributed to non-Møllers was found. It is listed in the table below.

$E_{Beam} = 3 \text{ GeV}$			$E_{Beam} = 4 \text{ GeV}$		
mat	thickness	backgr.(single arm)	mat	thickness	backgr.(single arm)
Fe	20 μm	1 %	Fe	20 μm	1 %
Fe	50 μm	3 %	Fe	50 μm	3 %

The background can be diminished by detecting the two Møller electrons in coincidence. The Monte Carlo simulation also showed that target thicknesses above 50 μm are not useful as multiple scattering blurs the spectra.

3. **Inelastic electron-interactions with the nucleus.** The scattering of highly energetic electrons off the nucleus also includes reaction channels like quasi-elastic scattering, the Δ -resonance excitation and deep-inelastic scattering. To calculate the contribution to the background, a program was used which is based on a model using y -scaling and a smeared deep-inelastic structure function.

⁴the basic code was written at UVa and consecutively extended by many users

The contribution from interactions with an iron nucleus is at maximum:

$$10\mu\text{barn}/(\text{MeV}\cdot\text{sr})$$

4. **Nucleon final state interactions.** When scattering highly energetic electrons off nuclei, hadrons can be knocked out of the target and find their way into the detectors. Although they can be differentiated from electrons by a clever detector they increase the number of triggers. The cross sections for finding a proton or pion are [OCLi]:

$$\begin{array}{ll} \text{e-p scattering} & 6.2 \mu\text{barn}/(\text{MeV}/c\cdot\text{sr}) \\ \text{e-}\pi \text{ scattering} & \text{negligible} \end{array}$$

Following conclusions can be drawn:

Given a Møller cross section of $Z \times 178 \text{ mbarn/sr}$, the background for single-arm scattering is dominated by the radiative tail of Mott scattering off the nuclei. When detecting the scattered and recoiling Møller electrons in coincidence the background can be reduced to an insignificant level.

2.5 Intra-atomic motion of bound electrons

The theory of Møller scattering is based on the assumption that the atomic electron is free and motionless. In reality, the inner (non polarized) electrons are more strongly bound than the (polarized) valence electrons, and have a momentum distribution that extends to much higher momenta.

Corrections related to these facts have been approximately calculated by Levchuk [Le92]. In summary, the polarized outer electrons can still be considered as free and motionless. For them the formalism of Møller scattering is valid. On the other hand, when scattering off the fast and strongly bound inner electrons⁵, the scattered electrons get a broadened angular distribution. These electrons will partly miss a detector with a small angular acceptance⁶, the ratio of the detected number of polarized to non-polarized Møller electrons increases. Upon calculating the beam polarization this finally leads to an overestimate of P_B .

For the large acceptances used in coincidence experiments the correction due to the intra-atomic motion of the electrons is small ($\leq 1\%$).

⁵which are not polarized

⁶or they will not be included in fits of the angular dependence which allow only for a narrow peak superimposed on a smooth Mott background.

Chapter 3

Møller target

This chapter first presents the traditional set up of a polarized Møller target. Then follows a second part presenting a new concept forming the base for measurements with higher precision.

Both target concepts have in common that they cannot measure directly the target polarization but calculate it out of target magnetization. Measuring target magnetization is closely linked to the way the target is polarized.

3.1 In-plane polarization

3.1.1 Set up of the target

All Møller targets so far are built in the manner presented here. Along the beam direction a pair of Helmholtz coils is set up. The Møller target, a thin foil of Supermendur (= a FeCoV-alloy), is placed between the coils. It is inclined at a small angle with respect to the beam (typically 20°).

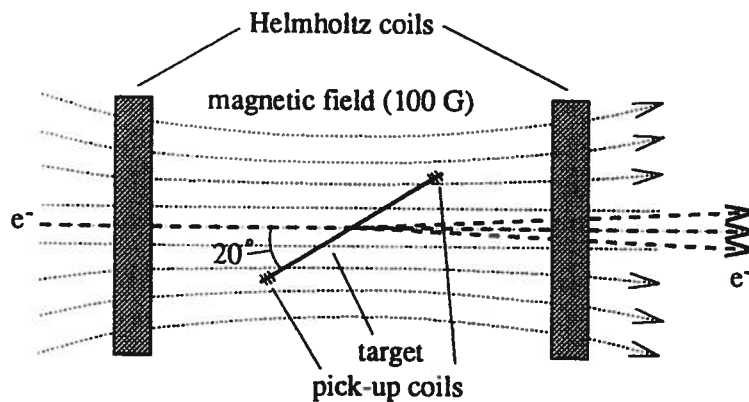


Figure 3.1: in-plane target set up

The target foil is described by 3 axes a, b and c, where a-b define the foil plane and c is perpendicular to this plane. With a magnetic field of 100 G produced by the Helmholtz coils, it is possible to magnetize the target to near saturation. The spins of the electrons are lying in the a-b plane of the foil. As the target is tilted with respect to the beam the target polarization has to be multiplied with the cosine of the tilt angle to get the component along the beam direction¹.

3.1.2 Extraction of target polarization

The magnetization of the target is measured with pick-up coils. At both ends of the target a coil is sewed into the foil. Upon reversal of the external magnetic field a voltage pulse is measured in the coils and integrated by a voltmeter. Two contributions to the measured peak area can be discriminated: first, the induction caused by the reversal of the external magnetic field and second, the signal produced by the flip of the electron spins. The two components are of similar magnitude. After subtraction of the first component (obtained by pick-up coil measurements without targets mounted in the frame) the remaining area under the peak is proportional to the number of flipped spins. The knowledge of the peak area ($=F$) and number of electrons leads then to the target polarization P via:

$$P = \frac{4\pi M}{K} \quad \text{with:} \quad 4\pi M = \frac{F_{\text{Foil in}} - F_{\text{Foil out}}}{\text{Area}_{\text{Foil}}} \quad ; \quad K = \frac{2\pi g'}{g' - 1} \cdot N \cdot \mu_B \quad (3.1)$$

where μ_B is the Bohr magneton, N the number of foil electrons and g' the magnetomechanical factor. The g' factor is not the one of free atoms but the corrected value for lattices ([Co75] uses $g' = 1.900 \pm 0.005$ for Supermendur, taken from [Sc67]). It is related to the electron g factor by $\frac{1}{g} + \frac{1}{g'} = 1$.

Although the method is quite simple there are a number of problems in practice. In the center of the target, where one is interested to know the polarization, it is not possible to place a coil as it would obstruct the beam. Therefore in a separate calibration run one has to install a third coil in the middle of the target and measure the ratio of the induction signals of the middle and end coils. This ratio middle/end is 1.05 - 1.1, depending on the foil thickness [Co75]. The lower value for the end coils arises from proximity to the end of the foil and inhomogeneities of the external field.

A further problem is related to the calibration of the peak area measurement. One has to know the number of electrons in the target. It can be calculated when knowing thickness, area, density and homogeneity of the target material. Thickness and homogeneity have to be determined experimentally by a γ -ray absorption experiment.

In experiments using beam currents larger than a few μA the Møller target is heated up at the beam spot. This heating leads to a local reduction of target polarization which is hard to control.

¹In the low energy regime, where $A_{zz} \neq 0$, measurements must be performed at positive and negative tilt angles in order to eliminate geometric asymmetries.

The pick-up coil method has the advantage to deliver an absolute value for the polarization; its drawback is related to the uncertainties connected to this kind of measurement. The target polarization measurement errors are today 3 % at best.

3.2 Out-of-plane polarization

The concept developed in this work is based on following ideas:

- The target is magnetically saturated. In this state it has a precisely known polarization and no measurement of polarization is needed a priori.
- The target saturation is continuously checked by observing the ellipticity of laser light reflected from the target (magneto-optical Kerr effect, see chapter 4). Besides proving saturation this method allows to measure relative changes of target polarization that could occur with beam on the target.

3.2.1 Set up of the target

The target is set up as shown in figure 3.2. The target consists of a foil of pure iron which is magnetically saturated in a 4 T field. The laser beam is used to prove the target saturation, as explained in more details in chapter 4.

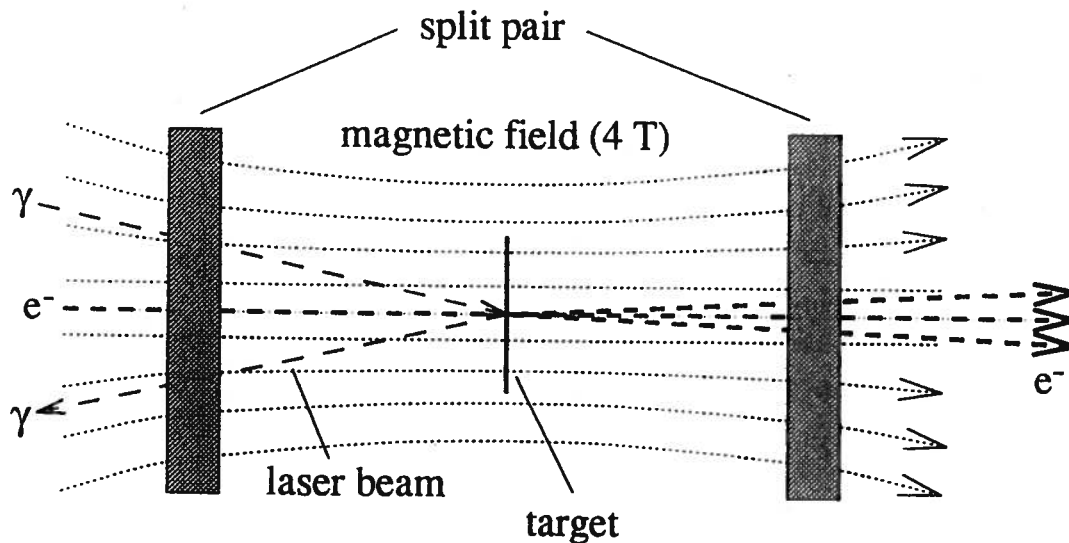


Figure 3.2: out-of-plane target set up

3.2.2 Magnetic saturation of the target

In absence of a magnetic field the electron spins of pure iron will lay in the foil plane and form Weiss domains. By applying an increasing magnetic field in c-direction more and more spins are forced to point out of the a-b plane. Upon the field exceeding the so-called saturation value, all spins are aligned along the field direction.

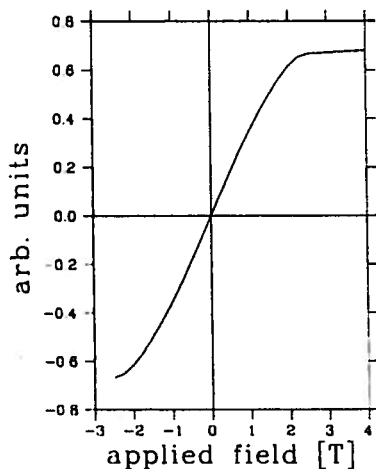


Figure 3.3 shows the magnetization curve of pure iron with a field applied perpendicularly to its surface. It was measured in a SQUID on one of our samples of 5 mm diameter and 20 μm thickness.

It is visible that even after saturation the curve continues to rise with a slight slope. The reason is that the saturation value at room temperature is inferior (97.8 %) to the saturation value at 0 K. This is due to the thermal vibration of the crystal lattice which hinders the electron spins to achieve perfect alignment. Only at 0 K or in an infinitely strong magnetic field this plateau would be perfectly horizontal.

Figure 3.3: magnetization out-of-plane of pure iron

3.2.3 Advantages of concept

The magnetization measurements with pick-up coils is limited by different factors mentioned in section 3.1.2. By saturating the target one gets a maximum value of the magnetization which is a property of the foil material only. This value has been determined in experiments that are far more precise than the pick-up coil arrangement. Two corrections must be applied to this value: The orbital motion of the electron produces a small but non-negligible contribution to the magnetization which must be subtracted. The result then must be corrected for demagnetization due to the finite target temperature. Both corrections are discussed in more detail in appendix B.

The laser (Kerr) device is needed to provide a relative measurement of the target magnetization. By proving that the target is indeed in saturation (i.e. by showing that an increase of the applied magnetic field does not lead to an increase of target magnetization) the target polarization can be calculated to very high precision as shown in appendix B. The Kerr device is also a useful tool to measure beam related depolarizations.

3.2.4 Possible target materials

All discussed materials have in common that they are ferromagnets. Thus one has to pay attention to the target temperature. Above the Curie-temperature T_C they display no

ferromagnetism. Between 0 K and $0.5 T_C$, magnetization decreases according to following law:

$$M_{Bulk}(T) / M_{Bulk}(0) \approx 1 - k \cdot T^{3/2} + (\text{higher terms})$$

Another point to be aware of is that an alloy has a magnetic behaviour that is different from the one of its individual elements.

Pure iron

Iron has not the highest polarizability of all ferromagnets, but it has the advantage to be well investigated. A large amount of experimental data about iron's magnetism are available. In a pure state (99.999 %) it has 2.216 ± 0.0008 free μ_B per atom which corresponds to a polarizability of $2.216/26 = 8.52$ % at 0 K. The Curie temperature is 770° C, magnetic saturation is reached at 2.2 T. Pure iron is easy to store. Due to missing impurities in the lattice (which serve as catalyst ions) pure iron does not oxidize.

Supermendur

Supermendur is an alloy consisting of $\text{Fe}_{49\%}\text{Co}_{49\%}\text{V}_{2\%}$. It is easily saturated in-plane and therefore serves as the classical target material. The Curie-point is approximately at 700° C. The Fe contributes $2.2 \mu_B$, the Co $1.7 \mu_B$. As Supermendur is an alloy the polarization must be calculated with help of the Slater-Pauling relation. In experiments the polarization of Supermendur has been measured to be ~ 8.3 %. Saturation out-of-plane needs approximately 2.2 T. Supermendur is sold by Vacuumschmelze Hanau under the name Vacoflux. It is rolled and has to be annealed to improve polarizability. The thickness of the foil varies by 5-10 %.

Gadolinium

This is a rare earth element which might be quite useful as a target. It has 7.9 free μ_B per atom resulting in a polarizability of $7.9/64 = 12.3$ %. The applied field for out-of-plane saturation is of the order of 2.6 T. The magnetic structure of Gd is fully isotropical, so out-of-plane polarization can be achieved without problems. However T_C is only 20° C. Thus a Gd-target has to be nitrogen-cooled to become a reasonable target. Gd oxidizes quickly and has to be stored in vacuum.

Dysprosium

Dysprosium has the highest polarizability with $10.6 \mu_B$ per atom resulting in 16.1 % polarization. The low Curie-point (88 K) requires helium-cooling, the large magnetic anisotropy makes it a difficult target.

Chapter 4

The Kerr apparatus

This section discusses the set up of the Kerr apparatus and briefly presents its individual components. In a last part specific problems of the device are discussed.

4.1 The Kerr effect

Once again it is emphasized that the target polarization can only be measured indirectly via its magnetization. The magnetic saturation of the target is measured using the magneto-optical Kerr effect¹. The Kerr effect terms the phenomenon that the polarization properties of light are altered in the presence of a magnetized medium. The principle of measurement is as follows: Linearly polarized light is reflected on a sample. The reflected

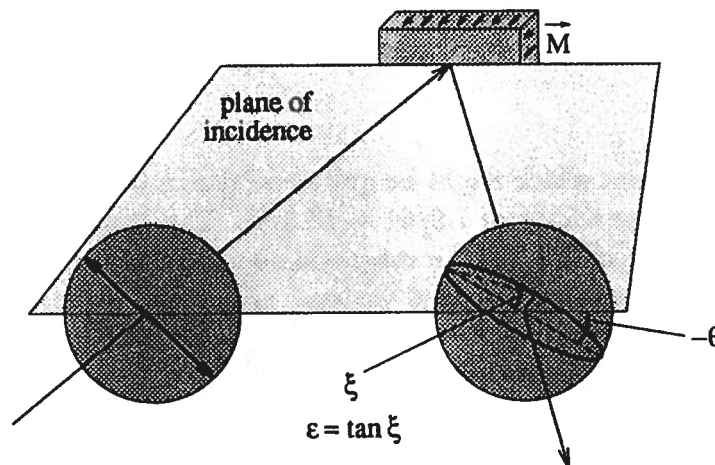


Figure 4.1: Principle of Kerr measurement

¹named after the scottish physicist John Kerr (1824-1907), pronounced 'kar', who first observed this effect in 1888. It is also referred to as MOKE, SMOKE.

light is still linearly polarized in the case the sample is not magnetized². On the other hand when the sample is magnetized the reflected light will become elliptically polarized and the polarization plane is rotated. The relative form of the polarization ellipsoid of the light can be fully described by two observables, the Kerr ellipticity ϵ and the Kerr angle θ . The change of these two observables with sample magnetization is in both cases linear [LL74]. In pure iron the maximum change of ϵ and θ are of the order of 0.2° .

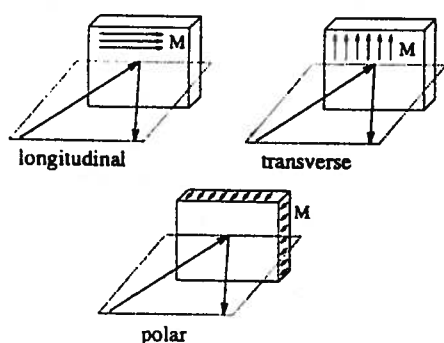


Figure 4.2: Kerr types

Three types of Kerr effects can be discriminated: polar, longitudinal and transversal (see figure 4.2 for their definition). The Kerr effect in the polar geometry is the easiest to measure, for two reasons: First, the polar component is one order of magnitude stronger than the two in-plane components. Second, when measuring in-plane, the separation of longitudinal and transverse components is difficult.

The mixing between in-plane and polar parts is negligible. Besides the suppression factor mentioned for the in-plane components, their contribution is proportional to the sine of the angle of incidence.

To deduce the magnetization of the sample one measures ϵ and/or θ as a function of the applied field. In the case of magnetization perpendicular to the plane (the 'hard' direction in iron) these functions do not display the typical separation between the magnetization branch up ($0 - 2.2$ T) and the branch down ($2.2 - 0$ T), commonly termed as hysteresis. Instead it is a single line with a constant slope which bends to a horizontal one at saturation (see figure 3.3). This unsplit curve demonstrates that no magnetization component out-of-plane is present in absence of an external H-field³. The more sensitive measurement of magnetization is obtained from the Kerr ellipticity ϵ .

The Kerr method gives no absolute polarization value. But the shape of the curve ϵ versus field yields the full information about the state of magnetization in the sample.

The Kerr signal originates from a zone that has a thickness of about twice the penetration depth of light. The depth after which the light intensity is reduced to $1/e$ is given by:

$$d = \frac{\lambda}{4\pi k} \quad (4.1)$$

where λ is the wavelength and k the absorption coefficient. For visible wavelengths, d of metals is typically 20 - 50 nm. The surface sensitivity of the Kerr method is not a drawback. Different experiments have proven that magnetization is always softer at the surface than in the bulk [Sc91, Ma88, Fr87, Al86, Pi82]. Saturation of the surface thus implies saturation of the bulk.

²Which is not absolutely true. The light will be elliptically polarized if the incidence angle is not 0° due to the different reflection coefficients for s- and p-waves. This is omitted for the sake of clarity.

³The typical split in hysteresis loops origins from domains not pointing into the direction of the magnetic field.

The basic tools to measure the Kerr effect are a monochromatic light source and two polarization filters. The incoming light is polarized by the first filter (= polarizer P) and then reflected on the non-magnetized target. The reflection passes a second filter (= analyzer A) which is crossed such that the throughput of reflected light is minimized. When the sample gets magnetized the polarization plane of the reflected light rotates, the amount of light passing the analysing filter is increased. Zeroing the light output again by turning the analyzer yields a new crossing angle. The angle difference between the old and new minima corresponds to θ . A similar method using a retardation plate after the polarizer is used to measure ϵ .

This method can be improved considerably by introducing a polarization modulator after the polarizer. The modulator sinusoidally varies the polarization state of the incoming light from left (LCP) to right (RCP) circularly polarized. The modulation frequency is 50 kHz. In the frame of circularly polarized light the Kerr effect can now be described as a difference in the refractive indices of the sample for RCP and LCP light. This generates ϵ and θ as is explained in appendix C.1. This difference in indices increases linearly with the magnetization of the sample.

Due to the modulation the detected light after the analyzer will not any longer be a DC-signal. Three dominant components can be discriminated:

- a DC-part which is proportional to the laser intensity
- an AC-component at the frequency of the modulator ($1f$), the amplitude of which is proportional to ϵ
- an AC-component at twice the frequency of the modulator ($2f$), the amplitude of which is proportional to θ

The advantages of the use of a modulator are:

- no moving parts
- resolution of ϵ and θ at least one order of magnitude better
- simultaneous measurement of ϵ and θ are possible (without using a $\lambda/4$ -plate)
- insensitivity to stray fields and room light
- possibility of automatization

The Kerr apparatus presented in the rest of this chapter includes a polarization modulator.

4.2 Set up

The set up is shown in figure 4.3. The space required for the optics is approximately 100×40 cm.

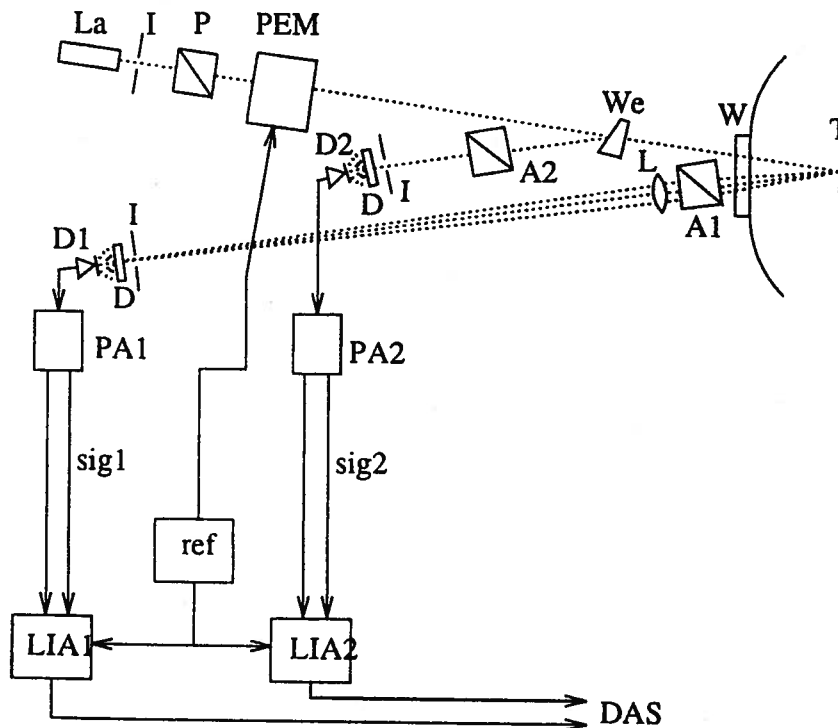


Figure 4.3: Kerr apparatus with components: laser diode incl. collimation lens (La), iris (I), polarizer (P), photo-elastic modulator (PEM) driven by the reference signal (ref), wedge (We), vacuum window (W), target (T), analyzers (A1,A2), focusing lens (L), diffusers (D), photodiodes (D1,D2), preamplifiers (PA1,PA2) each with an AC and DC output (sig1,sig2), lock-in amplifiers (LIA1, LIA2), data acquisition system (DAS)

The second detection arm (We-A2-D2) is installed in order to compensate temperature drifts of different components (see section 4.4).

4.3 Description of individual components

Laser diode (L)

The laser diode emits at 685 nm with a maximum power of 20 mW. A diode laser has inherent advantages compared to a HeNe laser used in the initial experiments:

- small dimensions, extremely long life-time (up to several 100'000 hours), low cost.
- System with integrated collimation optics are available off shelf.

- The laser intensity is monitored by a photodiode. The latter is directly integrated in the laser housing. The photodiode enables a feedback loop with the diode driver, resulting in an intensity stability of 0.05 %.
- The overall laser intensity can be regulated by the driver current. This is very convenient. First, saturation of the photodiodes is easy to avoid. Second, checking the linearity of the photodiodes over different intensity ranges can be performed without additional equipment (like gray filters).
- The laser spot is not round (as with HeNe lasers) but forms an ellipse with aspect ratio $\sim 1:2.5$. The electron beam is rastered in a similar shape over the target. Thus the two spots are matching in shape.

Of course the laser diode also has some drawbacks:

- The diode is extremely sensitive to current spikes.
- The laser intensity changes with temperature.

Iris (I)

The iris has an opening varying from 1 to 12 mm. It prevents reflected light from going back to the laser diode and removes unwanted halos. The insertion of an iris at the appropriate place has a significant impact on signal stability.

Polarizer (P), analyzer (A)

The polarizer improves polarization of the laser light and gives a defined polarization plane in the experiment. The analyzer transforms the magnetic information contained in the reflected light from a polarization observable into an intensity value.

The polarizers are Glan-Taylor prisms which achieve a high degree of polarization purity. Their extinction ratio when crossed is 10^{-6} . Power density should not exceed 200 W/cm^2 for the transmitted beam and 30 W/cm^2 for the absorbed part. Hence the incident laser spot should not be smaller than $0.25 \times 0.25 \text{ mm}^2$.

Photo-elastic modulator (PEM)

The PEM consists of a birefringent crystal, e.g. fused silica. Birefringence terms the fact that the two optical axis along the light propagation have different refractive indices. Linearly polarized light entering the crystal is split into its components along the two axes. As the components have different velocities in the medium (due to the different refractive indices), their phases differ at the end of the slab. At recombination the light is not any longer linearly but elliptically polarized.

4.3. Description of individual components

In order now to periodically modulate the ellipticity, a piezo crystal is glued at one end of the silica slab. Latter vibrates at 50 kHz, forming together with the slab a resonating device. The silica having a longitudinal vibration mode, the oscillating pressure changes

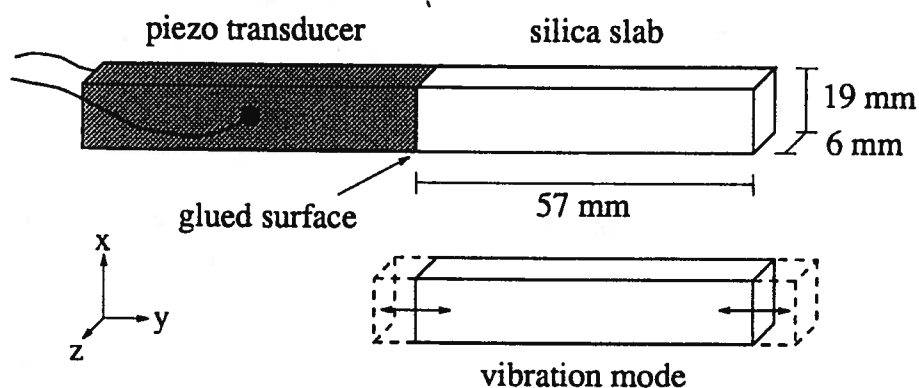


Figure 4.4: optical unit of the PEM

the refractive index only along the y-axis. Light incoming along the z-direction and linearly polarized at 45° with respect to the x- and y-axis of the PEM, is split into two equal components. The x-component travels untouched by the oscillatory motion, while the phase of the y-component changes sinusoidally. At recombination the laser light is modulated between right-handed and left-handed elliptically polarized light at 50 kHz.

The driver signal of the PEM is used as reference signal for the lock-in amplifiers.

Wedge (We)

The wedge extracts a fraction of the laser beam. This allows to monitor temperature influences on the PEM (see section 4.4). It is made from fused silica. The wedge angle is 4°, the extracted intensity is approx. 1 % of the total intensity.

Vacuum window (W)

The vacuum window is made of fused silica. A thin gold coating of a few nanometers at the inside prevents charging by low-energy secondary electrons.

Lens (L)

The laser light is reflected from the target into a cone. The lens focuses this cone onto the photodiode, thus maximizing light intensity and preventing measurement errors due to angular variations of the reflecting surface. The correct position of the lens is calculated according to $\frac{1}{f} = \frac{1}{s} + \frac{1}{s'}$ (where f is the focal length, s and s' the distances from lens to object and image respectively). The lens in use is of biconvex form.

Diffuser (D)

A diffuser scatters the incident light and so reduces the sensitivity of the detection system to slight positional changes. The most primitive diffuser is a piece of white paper. Another possibility is opal glass, which scatters into an almost ideal Lambertian sphere⁴.

Photodiodes (D1, D2)

The photodiodes measure the intensity of the light, their risetime is of the order of nanoseconds. They have been chosen because the reflected intensity is too high for photomultipliers.

Preamplifiers (PA)

Each preamplifier first duplicates the photodiode signal. In one branch the AC-part is amplified, in the other the DC-signal is formed, integrated over either 100 or 300 ms and amplified to a few volts. The gain factors of AC- and DC-branch are set independently. The AC-signal is fed into the signal input of the lock-in amplifier and is used to determine the Kerr signals. The DC-voltage is a measure of the laser intensity. It is digitized by one of the ADCs incorporated in the lock-in amplifier.

Lock-in amplifier (LIA)

Finding small AC-signals buried in large noise is made possible by the lock-in technique. The lock-in amplifier has two inputs, the AC-reference from the PEM driver and the signal coming from the preamplifier. The lock-in measures the frequency component of the preamplifier signal that matches the frequency of the reference signal. Locked onto this signal, a one-phase LIA displays the signal's amplitude, a two-phase LIA amplitude and phase.

Temperature monitors

Temperature sensors (not shown in figure 4.3) are placed on the PEM and the wedge. They consist of PT100 foil resistors. The readout units have a resolution of 0.1 K, generating a signal of 3.33 mV / 0.1 K on the monitor output. The latter is fed into an ADC of the lock-in amplifier.

⁴The name comes from the initial question by Lambert. He wondered why sunlight reflected from a wall produces a homogenous intensity distribution.

Data-acquisition system (DAS)

The lock-in amplifiers and the PEM driver are read out over RS232. Following data words are needed for the evaluation of the Kerr signals:

- 1f-signal of photodiode 1 ($= I_{1f}^{D1}$)
- 1f-signal of photodiode 2 ($= I_{1f}^{D2}$)
- DC-signal of photodiode 1 (converted by ADC at the back of LIA) ($= I_{DC}^{D1}$)
- DC-signal of photodiode 2 (converted by ADC at the back of LIA) ($= I_{DC}^{D2}$)
- temperature signal (converted by ADC at the back of LIA)
- further observables such as 2f-signals, solenoid field

The Kerr ellipticity is then calculated by $\varepsilon = I_{1f}^{D1} / (4 \cdot I_{DC}^{D1} \cdot J_1(\delta_0))$. For more details see appendix A, section A.3.2.

4.4 Hints and clues

Making a trivial device work is not always easy. Here different experiences and pitfalls are listed:

- Sturdy mounting of optical components is important, the whole device (incl. the target) must be mounted on one table. Inappropriate mountings lead to a sensitivity to building vibrations. The fingerprint of this problem is a signal 'oscillation' on the time scale of fraction of hours.
- Every optical interface generates a reflection carrying 1 – 4 % of the incident energy. These reflections must be removed by sending them back under small angles ($\sim 1^\circ$) and stopping them with help of irises or pin holes. Neglecting this can lead to a variety of problems:
 - A reflection going back to the laser results in extra energy deposited into the cavity, which disturbs its equilibrium state. The output intensity starts to 'breathe' on a time scale of ten minutes or more.
 - Laser light likes to interfere with itself, resulting in a cyclic variation of all signals.
 - A reflection reaching a photodiode leads to a nonsensical behaviour of its signal (e.g. the compensating arm measuring a variation linked to the magnetic field at the target).
- Analysis should happen as soon as possible after the target because conserving polarization through an optical set up is far more difficult than conserving intensity.

- Photodiodes are mechanically protected by a glass window. These windows cause interferences between the incoming beam and reflections from the window. To prevent this the windows must be removed. Some diodes have an extra protection consisting of a silicon droplet deposited on the surface of the semiconductor. This drop also disturbs signal measurement. Only photodiodes with a flat surface should be used.
- Photodiodes do not have a uniform response function over their surface. Slight positional changes of the beam can have a large impact on the measured signal. Sensitivity to this effect can be strongly decreased by using diffusers (see figure 4.5). The drawback is a reduction of signal intensity by a factor 10–100. This can be compensated by the use of preamplifiers.

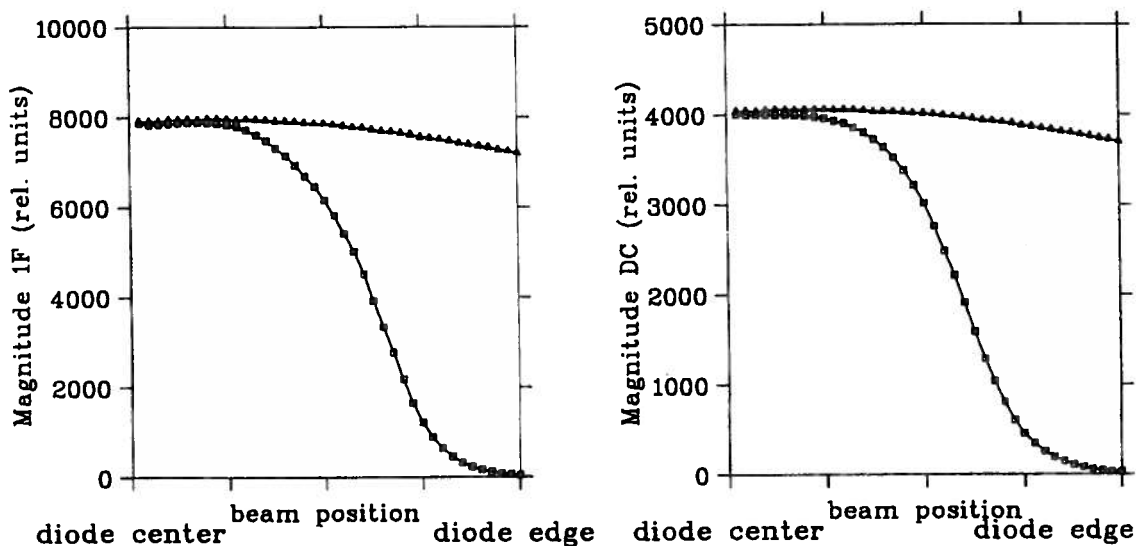


Figure 4.5: Diode response without diffuser (squares) and with diffuser (triangles). The diffuser response is multiplied by a factor of 80.

- The normal DC-shift observed in the photodiodes is in the range of a few tenths of % of its mean value. A DC-level constant within 0.2 % is a sign for saturation. In this case the laser intensity has to be decreased.
- The cable connecting photodiode and preamplifier is a powerful antenna. The normal coaxial shielding proves not sufficient. Therefore the photodiode should be integrated in the preamplifier housing. The latter then forms a faraday cage.
- Temperature effects are the only serious and large error source in this Kerr apparatus. For runs longer than 5 minutes, they cannot be neglected.

These effects are caused by inherent mechanical stresses in the PEM. Temperature acts on the amount of stress present in the material, thus altering the refractive indices along the two optical axes independently of the modulation process. Thus

changes of ϵ and θ are generated which are not due to magnetization in the target⁵. The PEM is specially sensitive to air flows, a first remedy is to put the entire device in a closed box.

It is possible to cut down considerably this effect by a simple procedure. A wedge introduced after the PEM extracts several beams from the main beam by reflection. Both the main and the extracted beam R2 are analysed separately in arm 1 and arm 2 respectively (see figure 4.3). The ellipticity ϵ measured in arm 1 is now affected by the PEM temperature and the target magnetization. On the other hand arm 2 sees only effects related to temperature. Division of the two (intensity normalized) 1f-signals yields a ratio R depending only on magnetization.

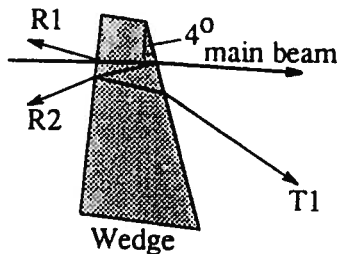


Figure 4.6: beam extraction in the wedge

Unfortunately R still has a slight dependence on temperature because the wedge also suffers from temperature induced stresses. This contribution is not fully canceled out when forming R . The reason is the different history lived in the wedge by the main beam and R2. The internally reflected beam R2 covers an extra distance in the wedge and undergoes an extra interaction at the upstream air-glass interface. The reflection coefficients at the interfaces, which differ for the s- and p-component, are influenced by the stress. Therefore the ellipticity ϵ of the internally reflected beam gets additionally distorted by the double-reflection⁶. The result is a slightly different reaction of R2 towards temperature induced stresses compared with the main beam.

Nevertheless this method compensates excellently smooth changes of ambient temperature. Under these circumstances the temperature dependent drift of R can be limited to 0.1 % over many hours. In contrast, sudden changes of temperature by some tenths of a degree arise the uncertainty level to 0.5 % (see also chapter 5).

Out of the three extracted beams shown in figure 4.6, R1 cannot be used. As it is generated by a surface reflection it does not carry the wedge temperature information. The beam R2 gives the best compensation signal. The angle between the incoming main beam and R2 should be as small as possible. The beam T1 is usable but has a lower intensity than R2. In addition, the extra interface deteriorates the precision of the compensation.

- After any major change of the mechanical set up, the optical system needs at least 12 hours before getting into an operational state. This is explained by all kind of tensions in the mountings and the optics which first have to get into an equilibrium.

⁵This effect has very little impact on the DC-signal, as the total amount of light throughput is in first order not dependent on birefringence.

⁶The extra path length of R2 compared to the main beam increases the phase difference between s- and p-component. This influences only θ .

After a sudden change of temperature in the range of a few degrees the device needs 4 - 5 hours to recover (see figure 5.3).

- Birefringence introduces a second problem. The birefringent components (PEM, wedge, vacuum window) introduce an offset ellipticity in the laser light. This has two consequences. First, an offset in the PEM yields a 1f-signal which depends not only on ε but also on θ (see appendix A, equation A.38). Second, it forces to run the lock-in amplifiers in an insensitive amplification range. The precision of resolving changes of magnetization diminishes. This offset ellipticity can be compensated by the insertion of a retarder ($\lambda/4$ -plate, Soleil-Babinet compensator) into the light path. Applying artificial stress perpendicularly with respect to the natural stress direction is also a possibility to zero the offsets.

Chapter 5

Measurements

This section presents results from different experiments performed with the Kerr apparatus. First the impact of temperature changes on the measured ellipticity ϵ as well as its compensation are shown. Then the ability to resolve changes of target magnetization is investigated. In the end a series of measurements shows the possibility to extend the Møller polarimeter to large beam currents by the use of a rotating target.

All these measurements were done with a prototype of the Kerr apparatus. The magnet in use was a conventional one and delivered a maximum field of only 0.45 T.

5.1 Temporal stability

The longest Møller runs are of the order of half an hour at a beam current of 10 nA. Temperature induced variations of the ellipticity must be minimized over these time scales, as they cannot be distinguished from effects related to the target magnetization. Figure 5.1 shows a measurement of long duration where the main beam was reflected on an aluminium mirror to exclude any change of ϵ due to target magnetization. On the top line the raw 1f- and DC-signals of arm 1 and 2 are shown. First the 1f-signals must be divided by the DC-signals to eliminate intensity drifts of the laser. The result is displayed on the second row. The ratio R is then formed on row 3. As magnetic information can be excluded in arm 1 (due to the Al mirror), the information carried in both arms is identical and the ratio should be a constant.

It is visible in figure 5.1 that stability is maintained over many hours within a very narrow limit. The compensating arm reduces sensitivity against temperature changes by a factor of the order of 5. The remaining variations and their relation to the environmental temperature are addressed in the next section.

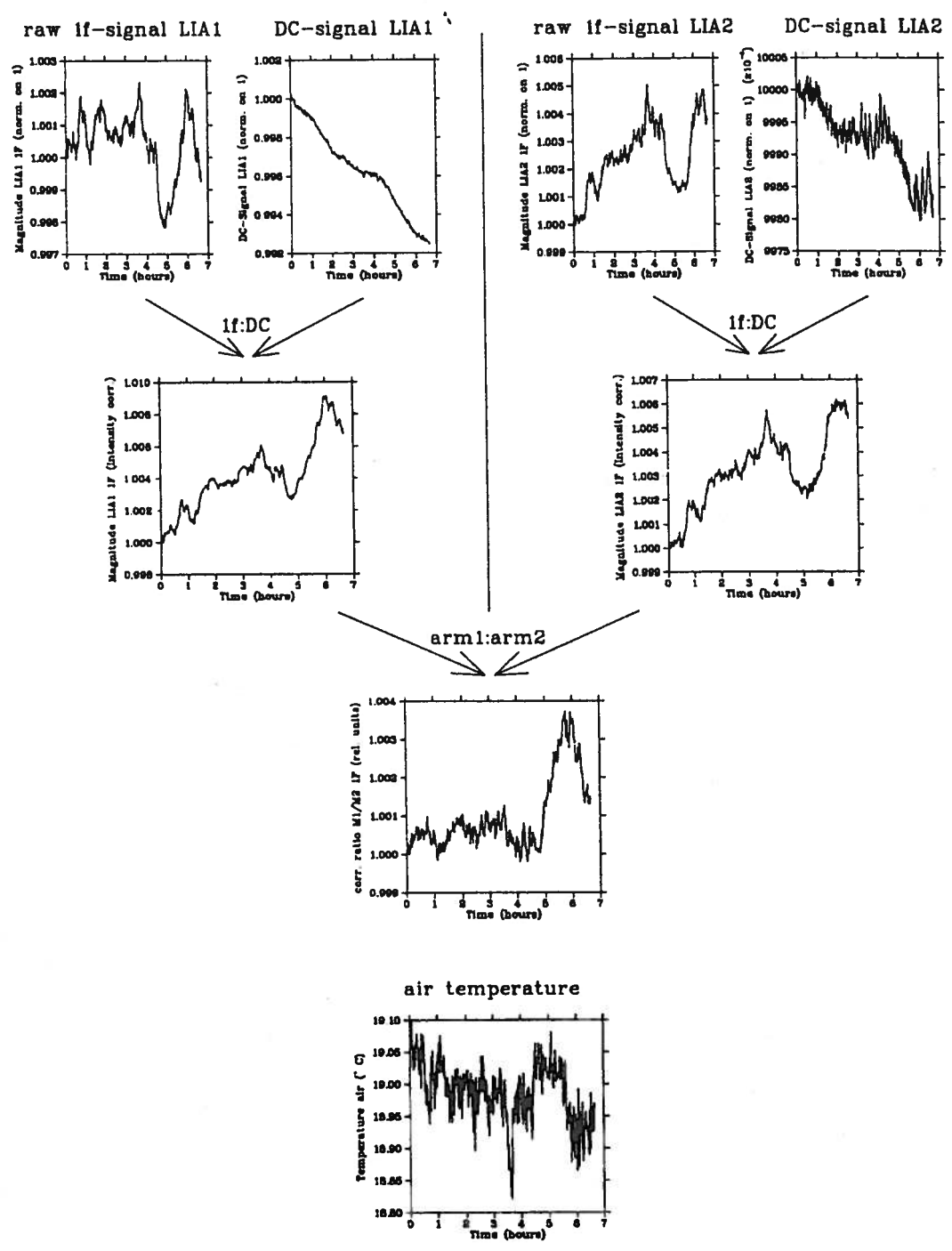


Figure 5.1: Signal stability of the Kerr apparatus

5.2 Temperature effects

The length of period over which temperature is changing is decisive for the quality of compensation. The influence of a small temperature change, which has both smooth and abrupt features, is shown in figure 5.2. A large change is presented in figure 5.3.

Figure 5.2¹ subsequently shows the corrected signal from the apparatus, the intensity corrected 1f-signals from arm 1 and 2 and the temperatures of air and modulator housing. It is obvious that the 1f-signals quickly react on air temperature fluctuations (see the correspondence with the dashed lines). Where fluctuations are very rapid the optics stay in their equilibrium. However the long lasting increase of temperature between the two dashed lines on the the very right leads to a new state in the wedge. This is visible by the changing ratio of arm 1 and arm 2 in the top picture. It is visible that air flows are responsible for this behaviour. The bottom picture shows the housing temperature of the modulator, which does not show any clear link with the variations of the 1f-signals.

Another interesting feature is that the smooth change of temperature by 0.1° in the first 4.5 hours is compensated within 0.1 % by the second arm. The nominally equal, but abrupt transitions at the hours 4.5 and 5.5 however deteriorate the quality of compensation.

Figure 5.3 shows the reaction to strong temperature changes. After 5.5 hours a heater in the box with the optics was turned on. The 1f-signals react with a drop by 17 %, the DC-signals and 2f-signals (both not shown) display rapid and large oscillations. In contrast the corrected signal drops only by 3 %. All signals become stable again at hour 10. Another few hours are needed to reach a final new equilibrium state ten hours after the start of the heating.

Conclusions are that the optics in the box must be kept at a stable temperature within 0.1° C. Abrupt temperature changes must be excluded, air flows must be stopped by walls within the box. In the case of a large temperature change the apparatus needs 6 hours to recover².

¹It represents the same run as figure 5.1

²Remember that in the case of changes in the mechanical set up this period is extended to 12 - 24 hours.

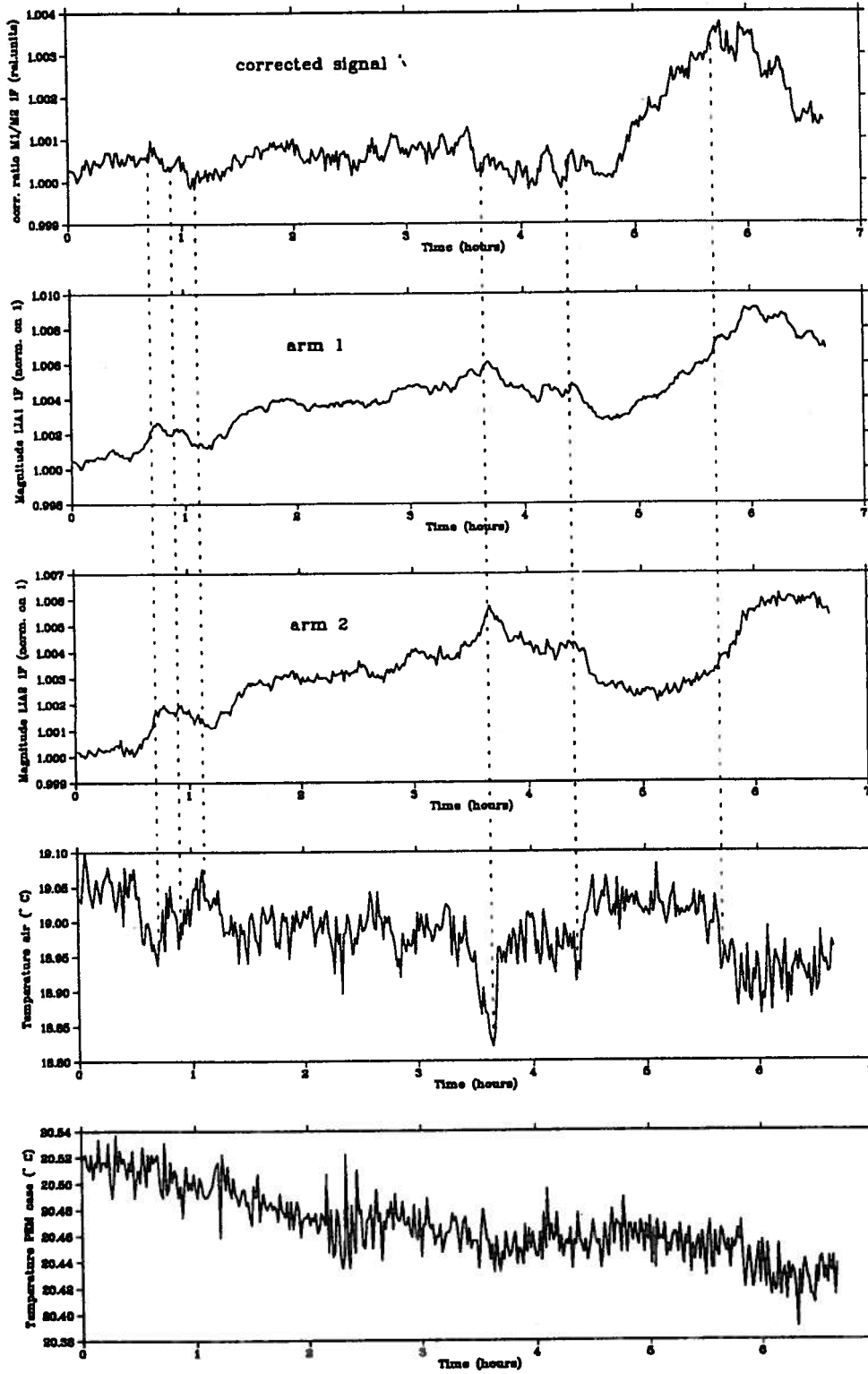


Figure 5.2: Sensitivity to small temperature fluctuations

5.2. Temperature effects

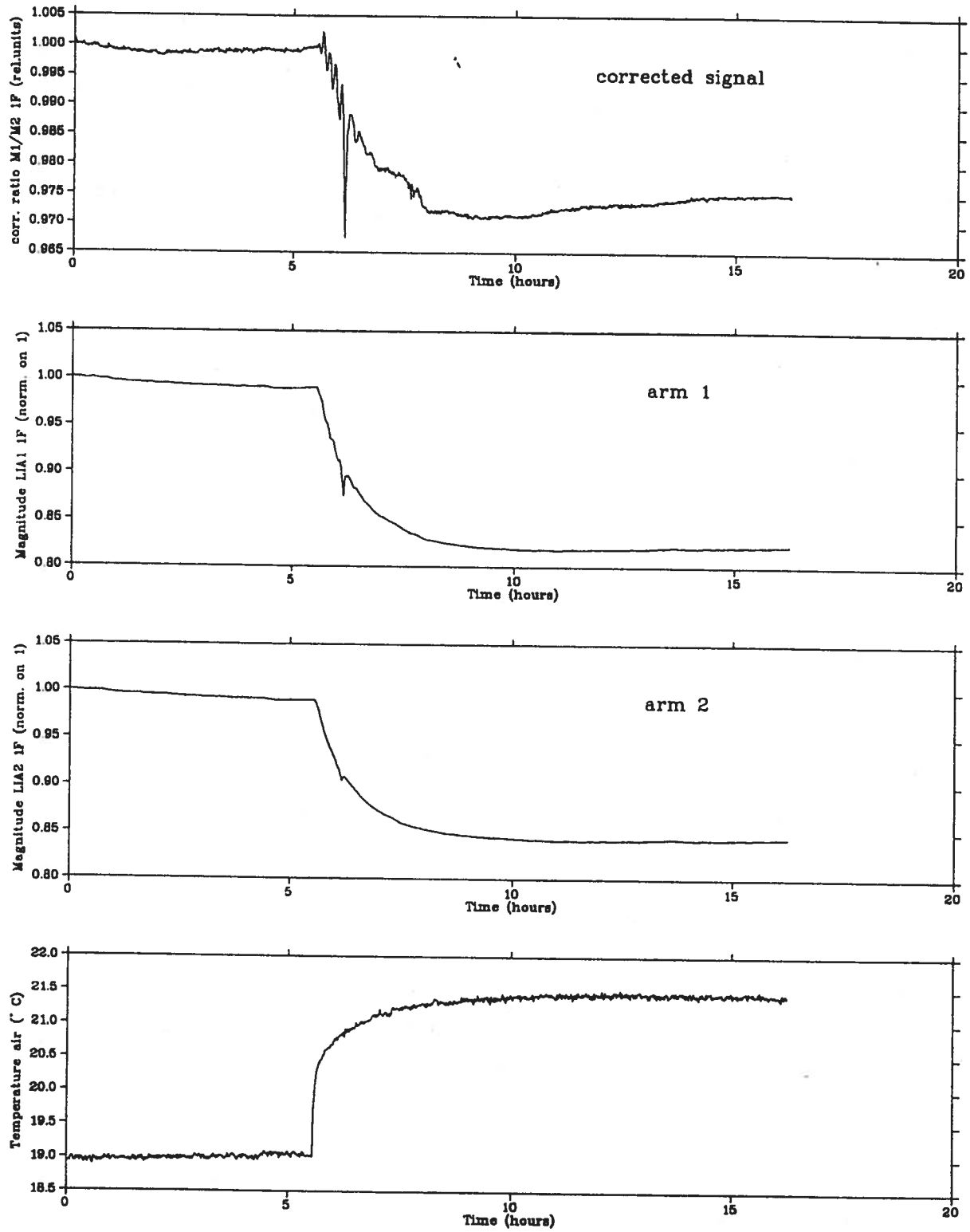


Figure 5.3: Sensitivity to large temperature changes

5.3 Kerr measurement

Figure 5.4 shows a hysteresis curve of a Supermendur target magnetized out-of-plane. As expected the data points show no different behaviour in an increasing and decreasing field. The maximum field applied is only a fifth of the saturation value, a saturated sample therefore yields a Kerr signal five times larger.

This measurement allows an estimation of the resolution of changes in the target magnetization. The difference of lock-in signal between zero and saturating field is extrapolated to 6500 units. The signal fluctuation being of the order of 10 units, a change of magnetization of approximately 0.2 % should be detectable. However the uncertainty due to temperature shifts is larger in most cases.

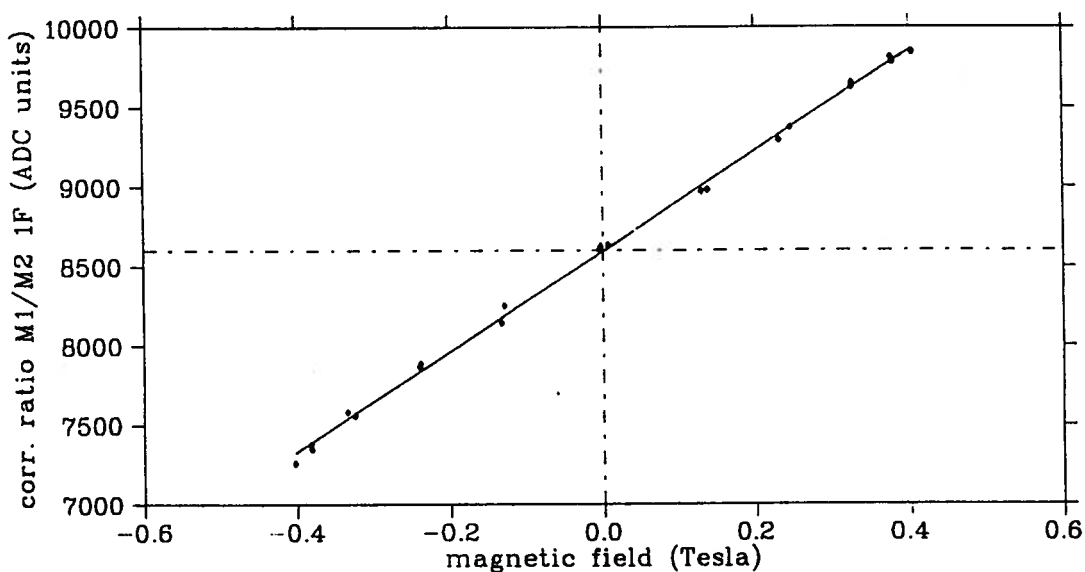


Figure 5.4: Kerr measurement of target magnetization

5.4 Target rotation

Figure 5.5 shows the behaviour of the 1f-signal in the case of a rotating target (see also section 6.4). With the target at rest the initial value corresponds to an ellipticity offset. This offset varies locally in the case where the target has not a perfectly smooth surface. When the target starts to rotate all the different offsets are integrated over by the lock-in amplifier with a time constant of 300 ms, resulting in an integrated offset value. It is obvious that this integral becomes smoother with increasing target rotation frequency. The small residual oscillations at 4 Hz are mainly due to the fact that the integration start and the target rotation were not synchronized.

The Kerr effect is also visible with a rotating target. The resolution of changes of magnetization is extrapolated to be 0.8 %, a value which can be improved by synchronizing target rotation and lock-in integration.

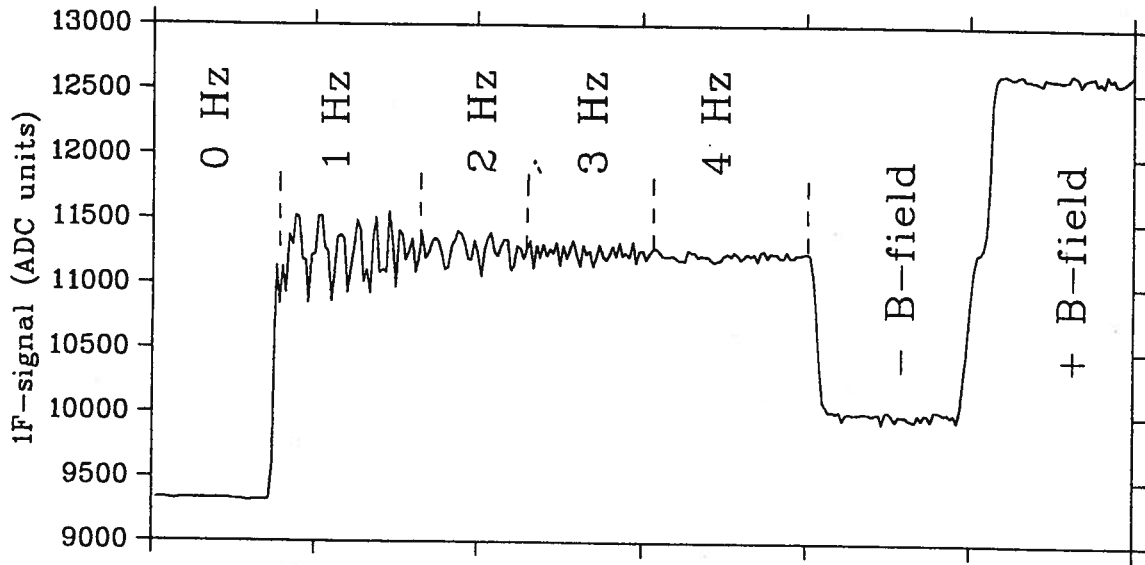


Figure 5.5: Kerr measurement of target magnetization

Although the offset values in figures 5.4 and 5.5 are different this has no consequences for the dependence of the 1f-signal on magnetization. Figure 5.6 shows an overlay of the 1f-signals of figures 5.4 and 5.5, the corresponding offset values have been subtracted. The change of signal in the static and the rotating target is identical. The reason that at zero field the diamonds are a bit below the dashed zeroline, whereas the squares are a bit above is the remanent field of the magnet. The sign of the remanent field depends on the direction of the last magnetic field produced.

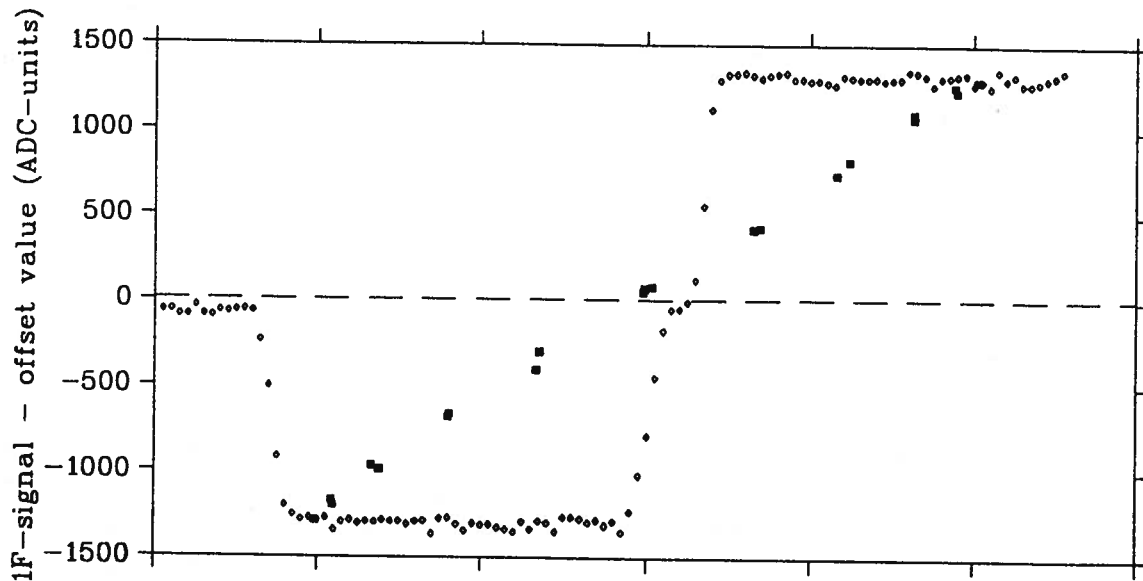


Figure 5.6: Change of the 1f signal of a stationary target (black squares) and a rotating target (diamonds) due to magnetization. Note that the units on the x-axis are different for the two measurements.

Chapter 6

Practical details

6.1 Measurement procedure

The measurement procedure for a Møller run looks essentially like this:

1. In the initial state there is no beam on the target and the magnet switched off. The 1f-signal measured now corresponds to an ellipticity offset. It should not exceed a few mV.
2. During the ramping of the magnetic field, the Kerr apparatus measures the hysteresis curve and proves the magnetic saturation of the target.
3. Measurement of the 1f-signal with beam on target allows to continuously monitor the target magnetization. A significant drop in the signal is the sign that the target is heated up locally.
4. Without beam and magnetic field the Kerr signals should come back to their initial offset value.

6.2 Target surface

The surface of the target foils has to be mirrorlike in order to produce a good reflection of the laser beam. This can be achieved by sputtering the target or polishing its surface. Sputtering gives a perfect surface but its drawback is the enclosure of sputtering gas in the target. The impurity is of the order of 0.5 %, enough to possibly change the magnetic properties of the target. Unfortunately only recently investigations were started to understand the influence of these inclusions on magnetization. Polishing does not allow to obtain an equal surface quality, but it is good enough. Best results were obtained by polishing first with very fine sandpaper, followed by 6 and 1 μm diamond paste on a rotating table. The polishing of a single target needs 1 – 2 days.

6.3 Multiple scattering in the target

Many of the Møller electrons will be multiply scattered before leaving the target. There is no easy analytic formula to describe the resulting angular distribution. A first approximation is a Gaussian distribution, the width σ expressed as ([PP90], p.116ff):

$$\sigma_{plane} = \frac{0.0141}{E(\text{GeV})} \cdot Z \cdot \sqrt{\frac{d}{L_R}} \cdot \left(1 + \frac{1}{9} \cdot \log \frac{d}{L_R}\right) \quad (6.1)$$

Z is the charge of the scattered particle ($=1$), d the target thickness ($20 \mu\text{m} \rightarrow 15.8 \text{ mg/cm}^2$), L_R the radiation length (iron = 13840 mg/cm^2). Multiplying σ_{plane} by 3 gives a full angle which contains approximately 95% of the scattered Møller electrons. The computation for three different energies yields:

E_{Beam} (GeV)	$3\sigma_{plane}$ (mrad, full angle)
2	0.5
4	0.25
6	0.2

The multiple scattering also leads to a general broadening of the main beam. If necessary this has to be compensated by a set of quadrupoles downstream of the polarimeter.

6.4 Power deposition in the target

A minimum ionizing electron deposits on average $2 \frac{\text{MeV}}{\text{g/cm}^2}$ in matter. Having an iron target with a density of $7.9 \frac{\text{g}}{\text{cm}^3}$, an electron will lose on average 1.6 eV per μm target thickness. One μA of beam being the equivalent of $6.242 \cdot 10^{10} \frac{e^-}{\text{sec}}$, the deposited power P in the target is:

$$P = 1.6 \text{ mW} \cdot \mu\text{m (Fe)} \cdot \mu\text{A (beam)} \quad (6.2)$$

The resulting temperature increase is crucially dependent on target geometry as most of the deposited energy is taken away by heat conduction. To estimate the temperature increase at the beam spot three different target geometries (as shown in figure 6.1) were investigated.

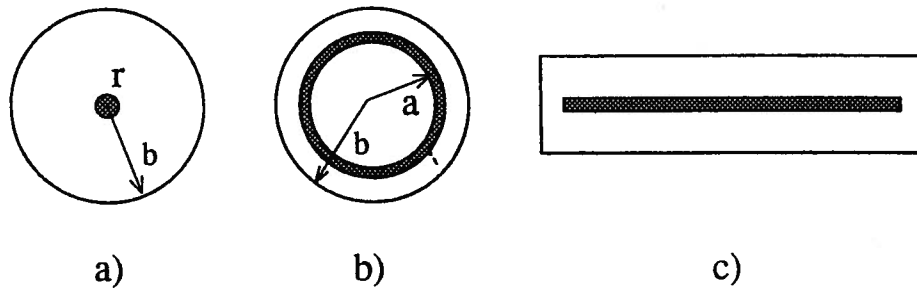


Figure 6.1: Target geometries, the beam deposits its energy in the shaded area

For all three target calculations, a constant temperature at the edge was used as boundary condition. Following constants were used throughout:

- k = thermal conductivity constant $\left[\frac{W}{cm \cdot K}\right]$
- r = radius beam spot $[cm]$
- b = radius target $[cm]$
- a = radius line $[cm]$
- q_o = deposited power per μm target thickness $[W]$
- c_p = specific heat capacity $\left[\frac{J}{g \cdot K}\right]$
- ρ = target density $\left[\frac{g}{cm^3}\right]$

6.4.1 Heating up of a round stationary target

For a round target hit centrally by the beam (figure 6.1 a), the temperature increase ΔT at the beam spot is given by:

$$\Delta T = \frac{q_o \cdot \ln(b/r)}{2\pi \cdot k} \quad (6.3)$$

While evaluating this formula one has to pay attention to the fact that the thermal conductivity constant k is a function of temperature. Roughly speaking it decreases with increasing temperature. The large influence of k is shown in following example calculated for a $20 \mu m$ iron target with a diameter of 2 cm and a beam spot diameter of 1 mm:

beam current	ΔT ($T_o = 20$ K)	ΔT ($T_o = 300$ K)
10 nA	0.01	0.2
100 nA	0.1	1.2
1 μA	1.0	12
10 μA	55	126

6.4.2 Heating up of a round rotating target

A rotating target is hit off center at a radius a by the beam, the target rotation frequency ν is large enough to assure uniform heat distribution (figure 6.1 b).

The heat distribution in a long solid cylinder with a heat source inside and a boundary kept at a constant temperature is [Öz89]:

$$T(r, t) = \frac{2}{b^2} \frac{\alpha}{k} \sum_{m=1}^{\infty} e^{-\alpha \beta_m^2 t} \cdot \frac{J_0(\beta_m r)}{J_1^2(\beta_m b)} \cdot \int_{t'=0}^t e^{\alpha \beta_m^2 t'} dt' \cdot \int_{r'=0}^b r' \cdot J_0(\beta_m r') \cdot g(r', t') dr' \quad (6.4)$$

where $\alpha = \frac{k}{c_p \rho}$
 $\beta_m \in \{\beta | J_0(\beta \cdot b) = 0\}, \beta_m = \left[\frac{1}{cm} \right]$

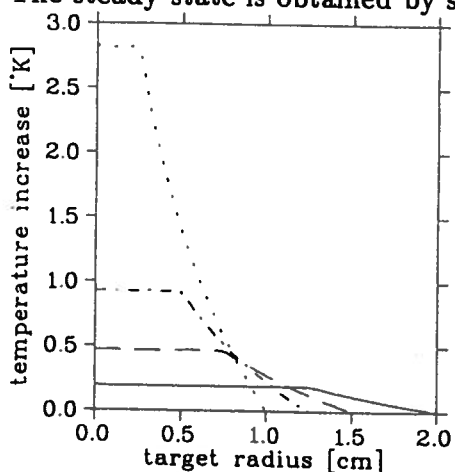
Now heat generation is restricted to the line drawn by the electron beam at radius a :

$$g(r', t') = q_0 \frac{\delta(r' - a)}{2\pi r'} \quad (6.5)$$

Putting this into equation 6.4 gives as result:

$$\frac{q_0}{\pi b^2 k} \sum_{m=1}^{\infty} \frac{J_0(\beta_m r) \cdot J_0(\beta_m a)}{\beta_m^2 J_1^2(\beta_m b)} (1 - e^{-\alpha \beta_m^2 t}) \quad (6.6)$$

The steady state is obtained by setting $t \rightarrow \infty$, the exponential function becoming zero.



The evaluation of the function leads to following conclusions: To keep the target at low temperature, the radius a drawn by the beam must be made as large as possible. The distance to the target edge should be minimized¹. The equilibrium temperature is reached after approximately 12 seconds. Figure 6.2 shows four temperature profiles as a function of the geometry. The sharp fall indicates the location of the beam spot at radius a . Its distance to the boundary was kept at 0.75 cm. The beam current is in all cases 1 μ A.

Figure 6.2: Temperature distribution in a round rotating target.

6.4.3 Heating up of a moving ribbon target

The temperature rise at the beam spot in a iron ribbon (figure 6.1 c) of infinite length, 2cm width and 20 μ m thickness was calculated with help of Green functions. The results can be presented in a simplified notation:

$$\Delta T(K) = 10^\circ \cdot \frac{I}{x} \quad (6.7)$$

¹In the case of CEBAF a minimal security distance between target frame and beam of 0.75 cm must be respected.

with $I =$ beam current (in μA)
 $x =$ length over which the beam spot is smeared (in cm)

This approximation is valid only for moderate temperature rises (for rises to 600°C insert 14 instead of 10 in the formula). After 10 seconds the equilibrium state is reached.

6.4.4 Radiation cooling

The emitted radiative power (in W) in a hemisphere is given by:

$$Q = c_s \cdot \epsilon \cdot A \cdot \left(\frac{T}{100}\right)^4 \quad (6.8)$$

with $c_s = 10^8 \cdot$ Stefan-Boltzmann constant $= 5.67 \cdot 10^{-4} \left[\frac{\text{W}}{\text{cm}^2 \text{K}^4}\right]$
 $\epsilon =$ emission coefficient of polished iron $= 0.15 [1]$
 $A =$ radiating surface = beam spot surface $[\text{cm}^2]$
 $T =$ temperature $[K]$

Evaluation of this formula shows that radiation cooling does not contribute significantly to the cooling of the target.

6.5 Eddy currents in a rotating target

As the magnetizing field has a small gradient over the target area, eddy currents are induced in a rotating foil. The power deposited is given by:

$$P = \frac{U^2}{R} = \frac{(l \cdot v \cdot \Delta B)^2}{R} \quad (6.9)$$

Thus P is determined by the square of the entrance/exit frequency and the experienced field change. Calculating P in a real material is not trivial as many material characteristics have to be considered. Using the tables in [Li85] the evaluation of a worst case target (iron of dimensions $5 \times 3 \times 0.002$ cm, entrance/exit frequency of 1 Hz through a 3 T field) gives a power deposition of $1 \mu\text{W}$.

Not to be neglected are forces exerted by the eddy currents. They must be taken into account when designing a rotating target.

6.6 Transversal polarization components

The spin direction of electrons leaving the source is rotated during the process of acceleration. Upon arrival at the main experimental target the electron spin is not necessarily purely longitudinal. Fortunately, the presence of transverse components diluting the experimental observables can be detected by the Møller polarimeter. With this information the electron spin at the source can be retuned such that it arrives purely longitudinal into the area.

How to obtain this information is shown in two different approaches. The first leaves the Møller target in a longitudinally polarized state, taking advantage of the large value of A_{zz} . The second uses a target with transverse polarization. This is a sensitive tool to measure the zero-crossing of transverse components.

6.6.1 Longitudinally polarized target

Turning the electron spin at the source by 360° while making consecutive measurements with the Møller polarimeter produces a longitudinal polarization function of the form:

$$P_z(\theta) = P_{z,max} \cdot \cos(\theta + \phi), \quad (6.10)$$

where θ is the spin direction at the source² and ϕ the unwanted phase introduced by the accelerator. Assuming that ϕ is zero, measurements at angles $+\theta$ and $-\theta$ must yield the same asymmetry. An unbalance in the values shows the presence of transverse components. The extraction of the correction ϕ from the unbalance is described in the following part. It is based on the idea, that the zero-crossing of the cosine-function is far easier to determine precisely than its flat maximum.

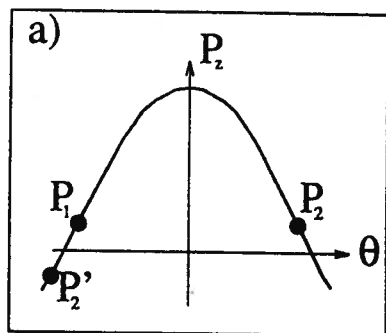


Figure a: The longitudinal polarization is measured e.g. for $\theta = -84^\circ$ and $\theta = +84^\circ$, yielding the results P_1 and P_2 . Assuming that $\theta \sim 0^\circ$ (i.e. the beam is nearly longitudinally polarized), P_1 and P_2 are approximately $0.1 \cdot P_{z,max}$. Due to the symmetry of the cosine function the transformation

$$P_2 = P_z(\theta + 84^\circ) = -P_z(\theta + 84^\circ - 180^\circ) = -P_2' \quad (6.11)$$

is valid.

²It is arbitrarily defined that a spin direction $\theta = 0^\circ$ at the source corresponds to full longitudinal polarization in the area.

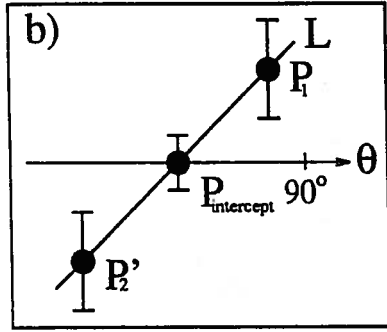


Figure b: The two data points P_1 and P_2' are joined by a straight line L of slope $m = 1$, a good approximation of the cosine around the intercept. The difference between the angle θ_0 at the zero-crossing of L and 90° corresponds to ϕ .

What are now the error bars allowed for P_1 and P_2' to pin down the intercept angle θ_0 to $\pm 1^\circ$? The mean of P_1 and P_2' yields the data point $P_{intercept}$ at the zero-crossing. Assuming that $\Delta P_1 \approx \Delta P_2'$ (which is valid in first order), the error law gives:

$$\Delta P_{intercept} = \frac{\Delta P_1}{\sqrt{2}} = \frac{\Delta P_2}{\sqrt{2}} \quad (6.12)$$

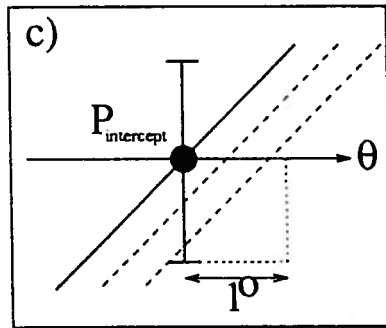


Figure c: The intercept line L can be shifted left or right by $\Delta\theta_0$ as long it stays in the error bars of $P_{intercept}$ (dashed lines). Linking $\Delta\theta_0$ ($= \pm 1^\circ = \pm 0.01745$ rad) to $\Delta P_{intercept}$ yields:

$$\Delta P_{intercept} = m \cdot \theta_0 = 1 \cdot 0.01745 \quad (6.13)$$

Combination of eq. (6.12) and (6.13) then results in:

$$\Delta P_{intercept} = 0.01745 = \frac{\Delta P_1}{\sqrt{2}} \quad \Rightarrow \quad \Delta P_1 = \sqrt{2} \cdot 0.01745 \quad (6.14)$$

As ΔP_1 on the right hand side of eq. (6.14) is a constant, the relative errors $\Delta P_1/P_1$ and $\Delta P_2/P_2$ vary with angle θ . For $\theta = 84^\circ$ they are 25%.

6.6.2 Transversally polarized target

To the left and right of the target a pair of Helmholtz coils is added. They polarize the target horizontally in-plane. As the target spins are now perpendicular to the longitudinal spins in the beam, no asymmetry is measured. However as soon as the beam has a horizontal component, an asymmetry appears. This method is sensitive as it measures the zero-crossing of a sine-function. The value of target polarization is of no interest in this context thus polarization measurements are superfluous.

Calculating rates is done as in section 2.3 but now using:

$$\frac{d\sigma}{d\Omega} = \frac{d\sigma^0}{d\Omega} (1 + A_{xz} P_z^B P_x^T + A_{xz} P_x^B P_z^T) \quad (6.15)$$

At higher energies A_{xz} vanishes for 90° CM. Thus³:

$$\frac{d\sigma}{d\Omega} = \frac{d\sigma^0}{d\Omega} (1 + A_{zx} (P_z^B \sin \phi) P_x^T) \quad (6.16)$$

³The same equation holds for measurements in \vec{y} -direction ($A_{xz} \rightarrow A_{yy}$, $P_x^T \rightarrow P_y^T$)

The value of A_{xx} being small ($-1/9$), this method becomes practical only at high beam currents and large deviation angles ϕ . For fixing the intercept the same ideas as in section 6.6.1 apply.

6.6.3 Measuring time

The measuring time for the two possible approaches is calculated with help of equation 2.24. It needs only a short calculation to see that the longitudinally polarized target is favoured by its large A_{zz} , which is seven times larger than A_{xx} . As long as the angle between beam and spin direction is not larger than 85° the longitudinal method is faster. Besides, this approach needs no extra device for producing a transversal polarization in the Møller target. However, it implies that at the source a spin rotator allows to turn the polarization by $\pm \sim 90^\circ$ with equal absolute value.

Chapter 7

Conclusions

Møller polarimetry has become nowadays a standard tool to measure electron beam polarization in accelerator experiments. The accuracy of the method, limited so far by uncertainties in the knowledge of target polarization and alignment, is at best 3 %.

This work presents a new way to deduce target polarization with a precision below 0.7 %. The troublesome pick-up coil measurements are avoided by magnetically saturating the target out-of-plane in a 4 T field. In a magnetically saturated specimen the polarization has been measured by experiments that are far more precise than the pick-up coil method. For an iron target at room temperature the polarization value is 7.981 ± 0.023 %.

To prove the assumption of magnetic saturation the magneto-optical Kerr effect is used. A Kerr apparatus has been set up and tested, its ability to measure magnetization has been proven. The relevant source of error in this device are temperature induced strains on the optics. The uncertainty introduced by smooth changes of temperature can be held below 0.5 % over many hours by the use of a compensating arm. The resolution of magnetical changes is expected to be of the order of 0.2 %, well below the uncertainty due to temperature. The use of the Kerr method also allows to observe beam related depolarization in the target and can extend Møller polarimetry to large beam currents by use of a rotating target.

Appendix A

Calculating optical properties with help of the Jones matrix calculus

The Jones matrix calculus is a convenient tool to calculate the transport of light through an optical system. It is valid as long as the system contains no depolarizing components. Making use of the periodic behaviour of waves the Jones matrix calculus projects the wave properties into complex space. The calculated results must then be converted back to real space in order to extract physical observables.

For more information on subjects treated in this appendix, see [Az88].

A.1 Phasor notation

In an undisturbed optical wave, each cartesian component of the electric vector varies sinusoidally, at all points in space. Under this condition, the amplitude A and the phase δ of the wave at different points in space are the only information to be sought. They can be lumped into a single complex quantity, the so called phasor.

A transverse plane wave at a fixed point in space can mathematically be represented by (in real space):

$$W = A \cos(\omega t + \delta) \quad (\text{A.1})$$

This can be expanded into complex space using the transformation $e^{ix} = \cos x + i \sin x$. The resulting time dependent term $e^{i\omega t}$ can be neglected during the matrix calculations as it is an understood, repetitive quality. Applied to the wave we get its (complex) phasor representation W_c :

$$W_c = A \cdot e^{i\delta} \quad (\text{A.2})$$

To recover the physical wave from the phasor W_c we first have to multiply it with the time-dependent term and then take the real part:

$$W = \text{Re}(W_c \cdot e^{i\omega t}) \quad (\text{A.3})$$

A.2 Matrix representation of polarized light

A plane wave with its plane of polarization perpendicular to its direction of propagation is fully described by 4 quantities: the azimuth θ , the ellipticity ϵ , the amplitude A and the phase δ .

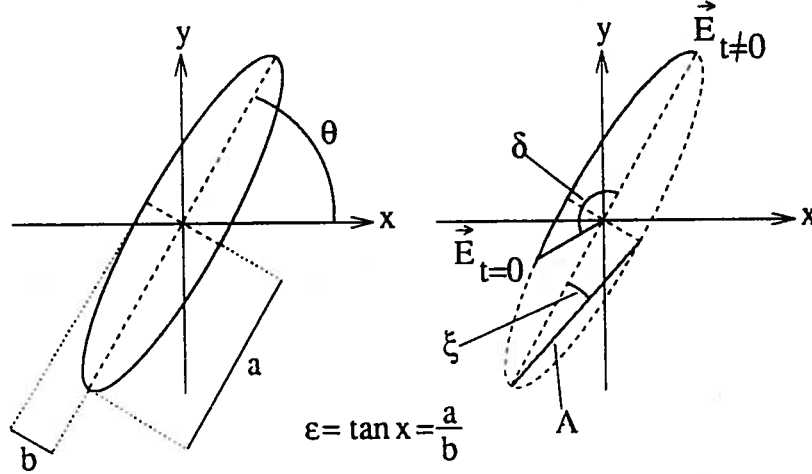


Figure A.1: The polarization variables θ , ϵ , A and δ . The direction of propagation z points towards the reader.

In a coordinate system where \vec{z} lies along the direction of propagation a transverse plane wave can be written as:

$$E(z, t) = \left[E_x \cos\left(\omega t - \frac{2\pi}{\lambda} z + \delta_x\right) \right] \vec{x} + \left[E_y \cos\left(\omega t - \frac{2\pi}{\lambda} z + \delta_y\right) \right] \vec{y} \quad (\text{A.4})$$

If \vec{x} and \vec{y} are matrix eigenvectors the expression can be simplified using matrix notation:

$$E(z, t) = \begin{pmatrix} E_x \cdot \cos\left(\omega t - \frac{2\pi}{\lambda} z + \delta_x\right) \\ E_y \cdot \cos\left(\omega t - \frac{2\pi}{\lambda} z + \delta_y\right) \end{pmatrix} = \begin{pmatrix} E_x \cdot e^{i\delta_x} \\ E_y \cdot e^{i\delta_y} \end{pmatrix} e^{-2\pi iz/\lambda} = \begin{pmatrix} E_x \cdot e^{i\delta_x} \\ E_y \cdot e^{i\delta_y} \end{pmatrix}_{z=0} \quad (\text{A.5})$$

The last term is the most general notation of a polarized wave.

A.2.1 Linear and circular polarization

The two most common bases for describing polarized light in matrix representation are cartesian and circular coordinates. The eigenvectors of the two systems are:

$$\epsilon_x = \begin{pmatrix} \cos \theta \\ \sin \theta \end{pmatrix}, \quad \epsilon_y = \begin{pmatrix} \sin \theta \\ -\cos \theta \end{pmatrix} \quad \text{cartesian} \quad (\text{A.6})$$

$$\epsilon_l = \frac{1}{\sqrt{2}} \begin{pmatrix} 1 \\ -i \end{pmatrix}, \quad \epsilon_r = \frac{1}{\sqrt{2}} \begin{pmatrix} 1 \\ i \end{pmatrix} \quad \text{circular} \quad (\text{A.7})$$

In the linear base θ denotes the angle between polarization and the \vec{x} -direction as defined in figure A.1. Values can be transformed between the two bases by use of the relationship:

$$\begin{pmatrix} E_l \\ E_r \end{pmatrix} = T \cdot \begin{pmatrix} E_x \\ E_y \end{pmatrix} = \frac{1}{\sqrt{2}} \cdot \begin{pmatrix} 1 & i \\ 1 & -i \end{pmatrix} \cdot \begin{pmatrix} E_x \\ E_y \end{pmatrix} \quad (\text{A.8})$$

$$\begin{pmatrix} E_x \\ E_y \end{pmatrix} = T^{-1} \cdot \begin{pmatrix} E_l \\ E_r \end{pmatrix} = \frac{1}{\sqrt{2}} \cdot \begin{pmatrix} 1 & 1 \\ -i & i \end{pmatrix} \cdot \begin{pmatrix} E_l \\ E_r \end{pmatrix} \quad (\text{A.9})$$

A.2.2 Elliptic polarization

In general a wave is elliptically polarized. Nevertheless describing this wave in a matrix system with elliptic eigenvectors is usually of little interest. In cartesian coordinates an elliptic polarization can be described by:

$$\begin{pmatrix} E_x \\ E_y \end{pmatrix} = Ae^{i\delta} \begin{pmatrix} \cos \theta \cos \varepsilon - i \sin \theta \sin \varepsilon \\ \sin \theta \cos \varepsilon + i \cos \theta \sin \varepsilon \end{pmatrix} \quad (\text{A.10})$$

and in circular coordinates we get:

$$\begin{pmatrix} E_l \\ E_r \end{pmatrix} = \frac{Ae^{i\delta}}{\sqrt{2}} \begin{pmatrix} (\cos \varepsilon - \sin \varepsilon) \cdot e^{i\theta} \\ (\cos \varepsilon + \sin \varepsilon) \cdot e^{-i\theta} \end{pmatrix} \quad (\text{A.11})$$

A.3 Calculations of this optical set up

In the optical calculations two kinds of coordinate systems are used, cartesian and circular. It is easier to understand the influence of certain optical elements by studying their influence in both coordinate systems. Usually the appropriate eigensystem to discuss the physical meaning of the results is the circular coordinate system.

In this section first the optical matrices used for the calculations are presented. In a second part the results for an ideal optical system are displayed followed by a last part discussing the effects introduced by different possible error sources.

A.3.1 List of optical matrices employed

• Matrix for an incoming beam, linearly polarized at an angle ϑ_E with respect to the \vec{x} -axis (see the definition of the axis in figure A.1):

$$E = \begin{pmatrix} \cos \vartheta_E \\ \sin \vartheta_E \end{pmatrix} \quad (\text{A.12})$$

Appendix A. Calculating optical properties with help of the Jones matrix calculus

- polarizer, analyzer at an angle $\vartheta_{P,A}$ with respect to the \vec{x} -axis:

$$P, A = \begin{pmatrix} \cos^2 \vartheta_{P,A} & \sin \vartheta_{P,A} \cos \vartheta_{P,A} \\ \sin \vartheta_{P,A} \cos \vartheta_{P,A} & \sin^2 \vartheta_{P,A} \end{pmatrix}_{\text{cart}} = \frac{1}{2} \begin{pmatrix} 1 & e^{2i\vartheta_{P,A}} \\ e^{-2i\vartheta_{P,A}} & 1 \end{pmatrix}_{\text{circ}} \quad (\text{A.13})$$

- Modulator at an angle ϑ_M with respect to the \vec{x} -axis, producing a retardation δ :

$$M = \begin{pmatrix} \cos \frac{1}{2}\delta + i \cos 2\vartheta_M \sin \frac{1}{2}\delta & i \sin 2\vartheta_M \sin \frac{1}{2}\delta \\ i \sin 2\vartheta_M \sin \frac{1}{2}\delta & \cos \frac{1}{2}\delta - i \cos 2\vartheta_M \sin \frac{1}{2}\delta \end{pmatrix}_{\text{cart}} \quad (\text{A.14})$$

The retardation δ produced by the modulator is $\delta = \delta_o \cdot \sin(2\pi \cdot \omega_M \cdot t)$, where δ_o is the modulator retardation amplitude (can be set at the control of the PEM) and the sine-term contains the modulation frequency ω_M of the PEM (50 kHz).

- Reflection-matrix of the target

$$R = \begin{pmatrix} R_p & R_{ps} \\ R_{sp} & R_s \end{pmatrix}_{\text{cart}} = \frac{1}{2} \begin{pmatrix} R_l & 0 \\ 0 & R_r \end{pmatrix}_{\text{circ}} \quad (\text{A.15})$$

$\begin{bmatrix} 1 & E-i\epsilon \\ \theta+i\epsilon & 1 \end{bmatrix}_{\text{cart}} \quad \epsilon, \theta \ll 1$
 $\begin{bmatrix} (1+i)(1-i) & 0 \\ 0 & (1-i)(1+i) \end{bmatrix}_{\text{circ}}$

The coefficients R_k are the Fresnel complex reflection coefficients. The fully written form is $R_k = r_k \cdot e^{id_k}$, where r_k is the ratio $\frac{\text{Amplitude reflected wave}}{\text{Amplitude incoming wave}}$ and d_k the phase shift upon reflection. For symmetry reasons the coefficients R_{ps} and R_{sp} are equal. Reflection polarization due to non normal angles of incidence is implicitly contained in R_k .

A.3.2 Diode response of an ideal optical system

The response of the Kerr device as seen by the diodes can be calculated by multiplying from right to left, in order of their appearance, the matrices of all individual optical components. The incoming polarized laser beam E goes through the polarizer P , is modulated by M , reflected at R and analysed by A . Calculating $A \cdot R \cdot M \cdot P \cdot E$ yields the wave W in front of the detector. The intensity of light I is then given by $W^* \cdot W$, where W^* is the complex conjugate of W .

Performing the multiplication, terms of the form $\sin \delta$ and $\cos \delta$ become omnipresent. They can be approximated by Bessel functions:

$$\sin \delta = \sin(\delta_o \cdot \sin(2\pi\omega t)) = 2J_1(\delta_o) \cdot \sin(2\pi\omega t) + \dots \quad (\text{A.16})$$

$$\cos \delta = \cos(\delta_o \cdot \sin(2\pi\omega t)) = J_0(\delta_o) + 2J_2(\delta_o) \cdot \cos(4\pi\omega t) + \dots \quad (\text{A.17})$$

These substitutions are quite useful because:

- the argument δ_o of the Bessel functions is the adjustable retardation amplitude of the PEM,
- the diode response signal is split up in frequency components. The desired frequency component can then directly be measured by the lock-in amplifier.

Calculations in linear coordinates

Performing the calculations and evaluating them for a set of angles $\vartheta_P = 90^\circ$, $\vartheta_M = 45^\circ$, $\vartheta_A = 0^\circ$ gives (angles are with respect to the \vec{x} -axis):

$$\begin{aligned}
I = |W|^2 = W^* \cdot W &= \frac{1}{2}(r_{ps}^2 + r_p^2) + \frac{1}{2}(r_{ps}^2 - r_p^2)J_0(\delta_o) && \text{DC-component} \\
&\quad \downarrow \quad \downarrow \\
&\quad 1 + \varepsilon^2 + \theta^2 \\
&+ 2r_{ps}r_p \sin(d_{ps} - d_p)J_1(\delta_o) \sin(2\pi\omega_M t) && \text{1f-component} \\
&+ (r_{ps}^2 - r_p^2)J_2(\delta_o) \cos(4\pi\omega_M t) && \text{2f-component}
\end{aligned} \tag{A.18}$$

Rotating the system by $90^\circ (\Rightarrow \vartheta_P = 0^\circ, \vartheta_M = -45^\circ, \vartheta_A = -90^\circ)$ and repeating the calculations yields an identical result, but with r_p being replaced by r_s . As the reflection coefficient r_s is always equal or larger than r_p (depending on the angle of incidence) this second set up is favorable. This is especially true for incidence angles far off the surface normal.

Calculations in circular coordinates

As the photo-elastic modulator transforms linearly into circularly polarized light, it is convenient to change after the PEM to a circular base. This is done by inserting the transformation matrix T given in equation [A.8]. The result of the multiplication $A \cdot R \cdot T \cdot M \cdot P \cdot E$ needs not to be transformed back to cartesian coordinates as the intensity of light is independent of the coordinate system. We obtain:

$$I = W^* \cdot W = \frac{1}{4}(r_l^2 + r_r^2 + (r_l^2 - r_r^2) \cdot \sin \delta - 2r_l r_r \cos(d_l - d_r) \cdot \cos \delta) \tag{A.19}$$

Inserting now the Bessel function approximation, the first three frequency components of our diode signal become:

$$I_{DC} = \frac{1}{4}(r_l^2 + r_r^2) - \frac{1}{2}r_l r_r \cos(d_l - d_r) \cdot J_0(\delta_o) \tag{A.20}$$

$$I_{1f} = \frac{1}{2}(r_l^2 - r_r^2) \cdot J_1(\delta_o) \tag{A.21}$$

$$I_{2f} = -r_l r_r \cos(d_l - d_r) \cdot J_2(\delta_o) \tag{A.22}$$

We can now link these three frequency terms to physical observables. The Kerr ellipticity ε and the Kerr rotation angle θ are defined as:

$$\varepsilon = \frac{r_l - r_r}{r_l + r_r} \tag{A.23}$$

$$\theta = \frac{1}{2}(d_l - d_r) \tag{A.24}$$

The beam intensity can be written as:

$$I = \frac{1}{2}(r_l^2 + r_r^2) \quad (\text{A.25})$$

As in general $r_l \approx r_r$ is true, we can use following approximations:

$$I = \frac{1}{2}(r_l^2 + r_r^2) \approx \frac{1}{4}(r_l + r_r)^2 \approx r_l \cdot r_r \quad (\text{A.26})$$

Inserting all these relationships in [A.20]-[A.22], our frequency terms transform into:

$$I_{\text{DC}} = +\frac{1}{2} \cdot I - \frac{1}{2} \cdot I \cdot \cos(2\theta) \cdot J_0(\delta_o) \quad (\text{A.27})$$

$$I_{1f} = +2 \cdot I \cdot \varepsilon \cdot J_1(\delta_o) \quad (\text{A.28})$$

$$I_{2f} = -I \cdot \cos(2\theta) \cdot J_2(\delta_o) \quad (\text{A.29})$$

The equations show that full information about the relative shape parameters ε and θ of the polarization ellipse can be obtained by measuring the I_{1f} - and I_{2f} -signals.

Changes in laser intensity I can easily be corrected for using following idea. The Bessel function J_0 is zero for an argument 137.8° . Putting the PEM retardation amplitude to this value gives a DC-signal which is only dependent on the laser intensity. The extraction of our two Kerr observables is now easy¹:

$$\varepsilon = \frac{I_{1f}}{4 \cdot I_{\text{DC}} \cdot J_1(\delta_o)}, \quad \theta = \frac{I_{2f}}{4 \cdot I_{\text{DC}} \cdot J_2(\delta_o)} \quad (\text{A.30})$$

A.3.3 Diode response of a non-ideal optical system

Looking at a system with angle settings $\vartheta_P = 0^\circ$, $\vartheta_M = -45^\circ$, $\vartheta_A = -90^\circ$ and a PEM-amplitude of 137.8° ($\Rightarrow J_0 = 0$), this section investigates the influence of different error sources on the three measured signals. The terms entering in addition to the terms presented for the ideal optical set up are underlined>. All calculations are performed in circular coordinates.

Analyser angle error

The analyzer is not crossed with respect to the polarizer ($\vartheta_A \neq \vartheta_P - 90^\circ$):

$$I_{\text{DC}} = \frac{1}{2} \cdot I + \frac{1}{2} \cdot I \cdot \cos(2\theta - \underline{2\vartheta_A}) \cdot J_0(\delta_o) \quad (\text{A.31})$$

$$I_{1f} = +2 \cdot I \cdot \varepsilon \cdot J_1(\delta_o) \quad (\text{A.32})$$

$$I_{2f} = +I \cdot \cos(2\theta - \underline{2\vartheta_A}) \cdot J_2(\delta_o) \quad (\text{A.33})$$

An error in the analyzer setting influences only the DC- and the 2ω -signals. The impact of an angle $\vartheta_A \neq -90^\circ$ is shown in figure A.2, where the observables ε and θ have been calculated as a function of ϑ_A using equation [A.30]. The graphs display the ratio of the non-ideal and the ideal results, also as a function of different values of θ .

¹assuming that $\cos(2\theta) \approx 2\theta$

A.3. Calculations of this optical set up

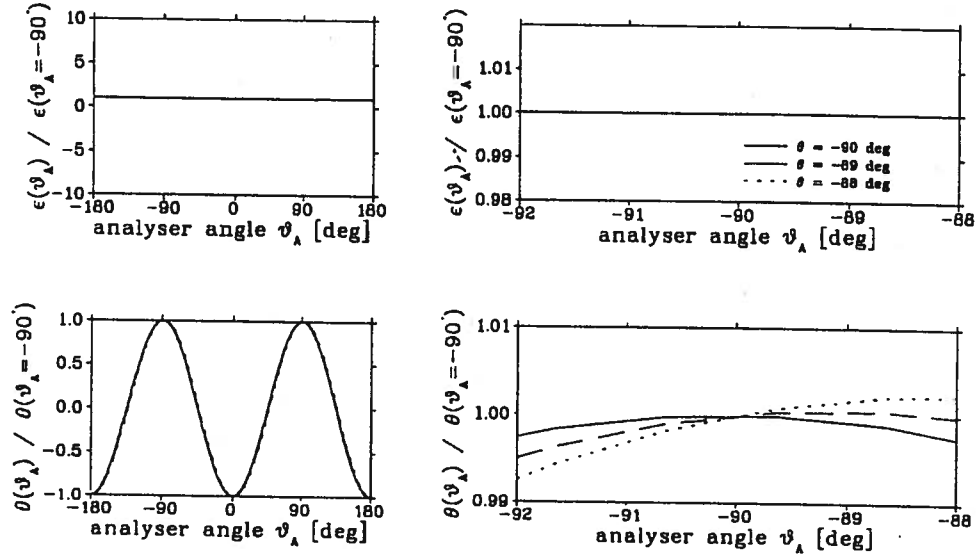


Figure A.2: error due to false analyzer setting

Modulator angle error

Setting the modulator at an angle $\vartheta_M \neq -45^\circ$ has following influence:

$$I_{DC} = \frac{1}{2} \cdot I + \frac{1}{2} \cdot I \cdot \frac{\sin(2\vartheta_M) \cdot \sin(2\theta + 2\vartheta_M) - \cos(2\theta)}{2} - \frac{1}{2} \cdot I \cdot \frac{\sin(2\vartheta_M) \cdot \sin(2\theta + 2\vartheta_M) \cdot J_0(\delta_0)}{2} \quad (\text{A.34})$$

$$I_{1f} = -2 \cdot I \cdot \frac{\sin(2\vartheta_M)}{2} \cdot J_1(\delta_0) \quad (\text{A.35})$$

$$I_{2f} = -I \cdot \frac{\sin(2\vartheta_M)}{2} \cdot \sin(2\theta + 2\vartheta_M) \cdot J_2(\delta_0) \quad (\text{A.36})$$

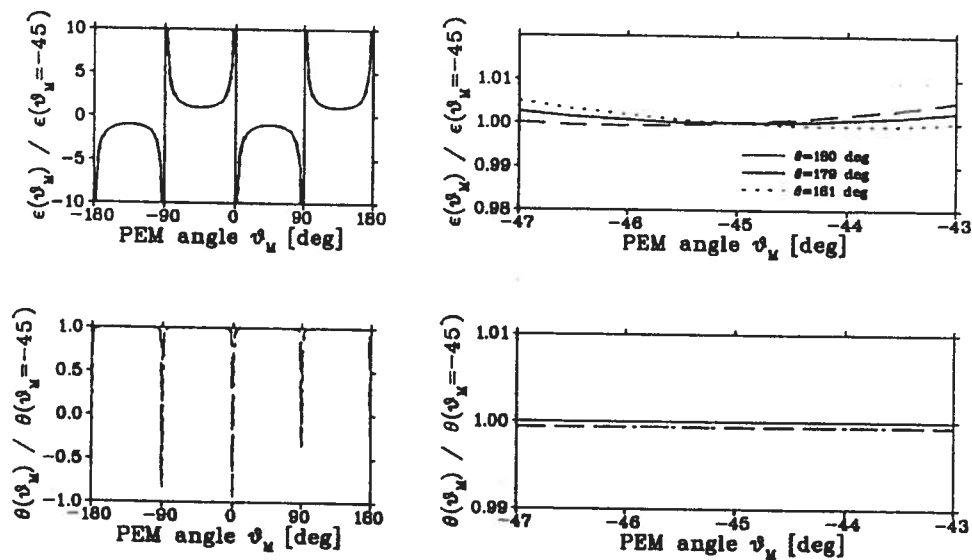


Figure A.3: error due to false modulator setting

Modulator retardation error

The retardation δ produced by the modulator is $\delta = \delta_0 \sin 2\pi\omega_M t + x$. The new term x denotes an offset retardation introduced into the modulator by resident stresses in the glass slab. The effect of x is:

$$I_{DC} = \frac{1}{2} \cdot I - \frac{1}{2} \cdot I \cdot \cos(2\theta) \cdot J_0(\delta_0) \cdot \cos(x) + I \cdot \epsilon \cdot J_0(\delta_0) \cdot \sin(x) \quad (A.37)$$

$$I_{1f} = +2 \cdot I \cdot \epsilon \cdot J_1(\delta_0) \cdot \cos(x) + I \cdot \cos(2\theta) \cdot J_1(\delta_0) \cdot \sin(x) \quad (A.38)$$

$$I_{2f} = -I \cdot \cos(2\theta) \cdot J_2(\delta_0) \cdot \cos(x) + 2 \cdot I \cdot \epsilon \cdot J_2(\delta_0) \cdot \sin(x) \quad (A.39)$$

It is important to note that in this case I_{1f} and I_{2f} are not any longer pure functions of ϵ and θ respectively.

Combined polarizer-analyzer angle error

Usually the polarizer and analyzer are crossed with respect to each other. Now if the polarizer is set at an angle $\vartheta_P \neq 0^\circ$, the crossed analyzer deviates from its ideal position by the same amount. In the following results the analyzer angle ϑ_A has been substituted by $\vartheta_A = \vartheta_P - 90^\circ$.

$$I_{DC} = \cos^2(\vartheta_P) \left\{ \frac{1}{2} \cdot I + I \cdot \sin(2\theta - 2\vartheta_P) \cdot \sin(\vartheta_P) \cdot \cos(\vartheta_P) - \frac{1}{2} \cdot I \cdot \cos(2\theta - 2\vartheta_P) \cdot \cos(2\vartheta_P) \cdot J_0(\delta_0) \right\} \quad (A.40)$$

$$I_{1f} = +2 \cdot \cos^2(\vartheta_P) \cdot \cos(2\vartheta_P) \cdot I \cdot \epsilon \cdot J_1(\delta_0) \quad (A.41)$$

$$I_{2f} = -\cos^2(\vartheta_P) \cdot \cos(2\vartheta_P) \cdot I \cdot \cos(2\theta - 2\vartheta_P) \cdot J_2(\delta_0) \quad (A.42)$$

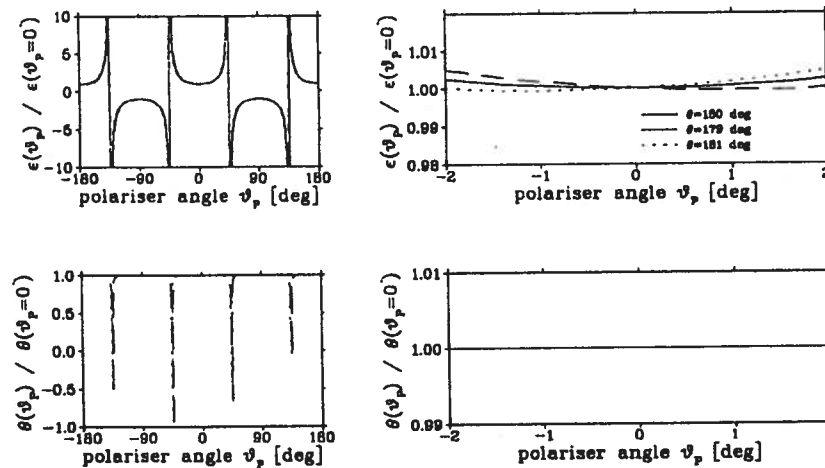


Figure A.4: error due to a false polarizer-analyzer setting

A.3. Calculations of this optical set up

The conclusion from these four error calculations is, that the setting of the optical elements in general is not very critical. The only critical case is the one of the modulator retardation error. Here the 1f-signal does not depend only on ϵ , but there is also a contribution from θ . The retardation of the PEM can be calibrated as described in the PEM user manual.

Appendix B

About magnetism

Calculating the polarization of a Møller target involves many magnetic properties not familiar to nuclear physicists. Therefore this appendix introduces basic concepts of ferromagnetism.

B.1 Free magnetic moments in ferromagnets

An electron in a free atom is described by four quantum numbers: (1) the total quantum number n which defines the orbit and its energy, (2) the orbital angular momentum l , (3) the spin angular momentum s and (4) the vector sum j of orbital and spin angular momentum. In the presence of a magnetic field also the spatial orientation of the orbit and spin momenta vector are quantized along the field direction (m_l, m_s). All the different orbits (defined by n, l, s, j) can only be occupied once (Pauli-principle).

Up to $Z=18$ (Argon) the atomic electrons are filled into shells in the order $1s, 2s, 2p, 3s, 3p$. Further increase of Z , however, results first in an occupation of $4s$ -levels. Only after that orbits in the $3d$ -shell are filled. This is due to the radial probability density of the $4s$ -orbit. It has a maximum in the vicinity of the nucleus while the $3d$ -wave has a node. Therefore the $4s$ -electrons are more strongly bound although on average they are more distant from the nucleus than the $3d$ -electrons. Investigations of ferromagnetic alloys show that the ferromagnetism of transition metals is related to elements with a $3d$ -shell occupied by 5 to 10 electrons.

Ferromagnetism depends mainly on the spin configuration of the electrons in matter. There are two main groups of theories trying to explain this relationship. The first assumes that the responsible electrons are localized at their respective atoms. This is especially useful for describing rare earth metals and ferrimagnetic oxides and compounds. The other theories use an itinerant electron model. The electrons responsible for ferromagnetism are thought of as wandering through the crystal lattice.

The mathematical formulation of the second model does not have simple solutions. First attempts have been undertaken by E.C. Stoner and J.C. Slater. It starts with an

investigation of the density of states in the 3d-band. Especially towards the Fermi level the density is very high. Each of these states can be occupied by two electrons, one with spin up, the other with spin down. In order to have a net magnetic moment, some electrons must be excited to higher energy levels and reverse their spin. Because of the high density of states, such an excitation needs little energy. The promoter of this excitation is the molecular field. The nature of this field was first presented by Heisenberg [He28]. Supposing there is an interaction between two atoms with spins \vec{S}_1 and \vec{S}_2 respectively, the potential energy is given by $W_{12} = -2J\vec{S}_1 \cdot \vec{S}_2$. J is called the exchange integral and derives as a direct result of the fact that the electrons must be indistinguishable. If J is positive, the potential energy is least for \vec{S}_1 and \vec{S}_2 parallel; if J is negative the stable configuration is that in which \vec{S}_1 is antiparallel to \vec{S}_2 . In order to have ferromagnetism, that is spins parallel, J must be positive. An examination of the Hamilton operator of the interaction potential shows that this condition is met when the interatomic spacing is large compared to the radii of the electron orbitals. Many more refined models have been used to extend this theory, but pursuing this topic goes beyond the frame of this short introduction.

As the resulting net magnetic moment is the difference between the magnetic moments of 3d-electrons with spins up respectively down, one would expect as result a multiple integer of μ_B . However, experiments show that the number of magnetic carriers is non-integral. Hartree-Fock calculations show that there is configuration mixing between the 3d- and 4s-shell. This leads to a nonintegral number of electrons attributed to each shell. Vonsovsky for example calculated 2.07 Bohr magnetons in the 3d-band, the 4s electrons contributing the rest. The world experimental data on the iron magnetic moment were reevaluated by [Da68], resulting in a

$$\text{magnetic saturation moment of iron (at } 0^\circ \text{ K)} = 2.2160 \pm 0.0008 \mu_B$$

B.2 The factors g and g'

For a more intuitive access to physics, derivations in this section are done within the classical framework. However some properties can only be derived when using quantum mechanical theories.

All atoms are carrying magnetic moments. A macroscopic magnetization is a sign that these magnetic moments are aligned. There are two possible origins of the atomic magnetic moment. One is the orbital motion of the electron around the nucleus, the other the electron spin.

An electron rotating around a nucleus will create a current $I = -e \cdot \frac{\omega}{2\pi}$ [A]. The magnetic moment M of a closed circuit with current I over an area F is $\mu_0 I F$ [Wb-m].

Thus the circular motion of the electron produces a magnetic moment:

$$M = \mu_0 \cdot \left(-e \cdot \frac{\omega}{2\pi}\right) \cdot (\pi r^2) = -\frac{1}{2} \mu_0 e \cdot \omega r^2 \quad (\text{B.1})$$

Using the angular momentum $p = m\omega r^2$ we can rewrite the formula as:

$$M = -\mu_0 \frac{e}{2m} \cdot p \quad (\text{B.2})$$

The angular momentum p of the orbit derives from quantum mechanics to be $p = n \cdot \hbar$. Therefore the magnetic moment generated by the orbital motion is:

$$M_L = -\mu_0 \frac{e}{2m} \cdot n\hbar \quad \text{with } n = 1, 2, \dots \quad (\text{B.3})$$

The smallest possible change of magnetic moment ($\Delta n = \pm 1$) is called the Bohr magneton

$$\mu_B = \frac{\mu_0 \hbar e}{2m} = 1.165 \cdot 10^{-29} \quad [\text{Wb}\cdot\text{m}] \quad (\text{B.4})$$

and equation B.3 can be simplified to:

$$M_L = -\mu_B \cdot n \quad (\text{B.5})$$

The magnetic moment M_S induced by the spin can be calculated in a similar manner, taking in account that the quantization of the spin is $\hbar/2$. It is immediately visible that this would imply the existence of a quantum of magnetization of 1/2 of a Bohr magneton. Experiments show that this is not possible. The classical treatment evades at this point the problem by introducing ad-hoc the g -factor¹:

$$M_{L,S} = -g \cdot \mu_B \cdot n \quad \text{with } g = 1 \text{ for orbital motion and } 2 \text{ for spin rotation} \quad (\text{B.6})$$

The above values are only true for free atoms. In solids the orbital wave functions become distorted by the lattice. The measurement of the g -value in matter therefore reveals whether a macroscopic magnetization is due to contributions from the orbital motion ($\rightarrow g = 1$) or the spin ($\rightarrow g = 2$).

The g -factor can be measured using the ferromagnetic resonance. These experiments are similar to nuclear or electron spin resonance experiments. The ferromagnetic sample is brought into a strong magnetic field. Assuming that the field is large enough to saturate the sample the process can be viewed as the precession of the total magnetic moment in the field. The precession frequency is given by [Mo80]:

$$\omega = -\frac{g \cdot \mu_B \cdot H_{\text{effective}}}{\hbar} \quad (\text{B.7})$$

¹A correct derivation of the g -factor follows from QED (Dirac-equation). It shows that the g -value of the spin is 2.002, due to radiative corrections (γ -selfinteraction). This is also measured in experiments.

From the value of $H_{effective}$ at the resonance frequency, the g -factor can be extracted. It is possible to show in that context [Mo80] that

$$g = \frac{L + 2S}{S} \quad (B.8)$$

where L and S are the expectation values of the atomic orbital and spin angular momenta.

Another way to determine the magnetic contributions of M_L and M_S in ferromagnets exploits a magneto-mechanical effect: rotation by magnetization (Einstein-de Haas effect). To this end a ferromagnetic rod is suspended inside a solenoid. It is fixed on a torsional pendulum which measures a rotation of the rod about the magnetic axis of the solenoid. When changing the rod magnetization, an angular momentum about the magnetic axis is observed. The experiment is very delicate to perform, as it is also sensitive to variations of external magnetic fields. A summary is given by [Sc62]. The experiment measures the magneto-mechanical ratio defined as:

$$g' = \frac{\text{change of magnetization}}{\text{change of angular momentum}} \cdot \frac{2mc}{e} \quad (B.9)$$

It can be shown that above equation is equivalent to

$$g' = \frac{L + 2S}{L + S} \quad (B.10)$$

Besides producing results of high precision the approach is very direct, avoiding theoretical manipulations of the results.

Combination of equations B.8 and B.10 gives the important relationship

$$\frac{1}{g} + \frac{1}{g'} = 1 \quad (B.11)$$

The experimental values of g and g' for pure iron are [Re69]:

$$g(\text{Fe}) = 2.091 \pm 0.015 \quad , \quad g'(\text{Fe}) = 1.919 \pm 0.002$$

It is obvious that g' is more accurately determined (which has to do with the experimental procedure). The extraction of the orbital contribution to the total magnetization is now given by $M_{Orbit}/M_{Total} = (2 - g')/g'$ and leads to an

**orbital contribution to the magnetic saturation moment of iron
(at 300 K) =**

$$0.0918 \pm 0.0033 \mu_B = 4.22 \pm 0.15 \%$$

Before converting magnetization to spin polarization this contribution must be subtracted.

B.3 Magnetization and temperature

The saturation magnetization of a ferromagnet is a temperature dependent property. With increasing temperature, the thermal motion of the material lattice disturbs a perfect alignment of the electron spins and thus lowers the observed magnetization. Table B.1 shows the magnetization of iron as a function of temperature (interpolated from data in [Ha72]). The values are normalized with respect to the value at 0 K .

Temperature (K)	rel. polarization (%)	Temperature (K)	rel. polarization (%)
0	100	620	90.2
273	98.2	670	88.1
290	97.9	720	85.5
300	97.8	770	82.6
320	97.3	820	78.5
370	96.1	870	72.2
420	94.9	920	64.8
470	94.0	970	50.0
520	93.0	1020	19.2
570	91.8	1043	0.00

Table B.1: magnetization vs. temperature

B.4 Iron polarization at room temperature

The values compiled in the previous sections are used here to calculate the polarization of electrons in pure iron at 300 K. The 0 K saturation value P_0 is corrected to the one for 300 K using the factor C_{300} , the orbital contribution O_{300} at 300 K is then subtracted to get the spin contribution M_S to the magnetic moment:

$$M_S = P_0 \cdot C_{300} - O_{300} \quad (\text{B.12})$$

$$\Delta M_S = \sqrt{(C_{300} \cdot \Delta P_0)^2 + (P_0 \cdot \Delta C_{300})^2 + (\Delta O_{300})^2} \quad (\text{B.13})$$

Taking the values $P_0 = 2.2160$, $\Delta P_0 = 0.0008$, $C_{300} = 0.978$, $\Delta C_{300} = 0.002$, $O_{300} = 0.0918$, $\Delta O_{300} = 0.0033$, one gets the

B.5. Conversion table of magnetic quantities

spin contribution to the magnetic moment of saturated pure iron
(at 300 K):

$$M_S = 2.075 \pm 0.006 \mu_B$$

and expressed in terms of target polarization:

$$P_{Target} = \frac{M_S}{26} \Rightarrow 7.981 \pm 0.023 \%$$

B.5 Conversion table of magnetic quantities

Quantity	Symbol	SI-units	cgs-units	$\frac{\text{SI-value}}{\text{cgs-value}}$
magnetic induction	B	1 Tesla (= 1 V s m ⁻²)	10 ⁴ Gauss (= 10 ⁴ g ^{1/2} cm ^{-1/2} s ⁻¹)	10 ⁻⁴
magnetic flux	Φ	1 Weber (= 1 V s)	1 Maxwell (= g ^{1/2} cm ^{3/2} s ⁻¹)	10 ⁻⁸
magnetic field	H	1 Ampère / meter (= 1 A m ⁻¹)	1 Oersted (= g ^{1/2} cm ^{-1/2} s ⁻¹)	$\frac{1}{4\pi} \cdot 10^3$
magnetization	M	1 Weber / m ²	1 Gauss	4π · 10 ⁻⁴
magnetic moment	μ _B	Weber · m		4π · 10 ⁻¹⁰

Table B.2:

B.6 Magnetic relationships in matter

		SI-units	cgs-units
magnetic induction	$\vec{B} =$	$\mu_0(\vec{H} + \vec{M})$	$\vec{H} + 4\pi\vec{M}$
magnetization	$\vec{M} =$	$\chi_m \vec{H}$	$\chi_m \vec{H}$
susceptibility	$\chi_m =$	$\mu - 1$	$\frac{\mu - 1}{4\pi}$
Bohr magneton	$\mu_B =$	$\frac{e\hbar}{2m_e}$	$\frac{e\hbar}{2m_e c}$

Table B.3:

Appendix C

Theoretical explanation of the Kerr effect

To understand the origin of the Kerr effect two different approaches are used. First the theory of wave properties in matter leads to a macroscopic description, then an atomistic explanation is given.

C.1 Macroscopic description

Before explaining the generation of the Kerr effect, different optical properties of media are discussed. The following explanations are all macroscopical descriptions and therefore only valid as long as the wavelength of the incident electromagnetic wave is much larger than atomic dimensions. For furthergoing explanations see [LL74].

Dispersion of ϵ and μ in media

If a material is a conductor and an electromagnetic field varying over time is applied, the permittivity (or dielectric tensor) ϵ and the magnetic permeability μ are functions of the field frequency. The law describing the functional dependence on ω is called the dispersion relation.

The induction and field strength produced by an electromagnetic wave incident on a medium are best described by tensors:

$$D_i = \epsilon_{ik}(\omega) \cdot E_k, \quad B_i = \mu_{ik}(\omega) \cdot H_k \quad \text{with } i, k = x, y, z \quad (\text{C.1})$$

In the low frequency regime ($\omega \rightarrow 0$) the tensors get their static values ϵ and μ respectively. For high frequencies ($\omega \rightarrow \infty$) the tensors loose their physical meaning and are set to 1. The limiting frequencies for $\epsilon_{ik}(\omega)$ and $\mu_{ik}(\omega)$ are different. For $\epsilon_{ik}(\omega)$ it is in the region of ultraviolet light. There the wavelength is of the order of atomic dimensions. The atom does not sense any longer a homogeneous electrical field, therefore the macroscopic

description is not applicable. The physical meaning of $\mu_{ik}(\omega)$ vanishes already below optical frequencies. The reason is the long magnetical relaxation time in ferromagnets. A change of magnetic moment induced by a changing outer field H can only happen when H does not vary much faster than the relaxation time. Therefore one sets

$$\mu = 1 \text{ at optical frequencies}$$

The refractive index

A monochromatic wave travelling through a homogeneous medium is described by the Maxwell equation:

$$\Delta \vec{E} + \varepsilon \mu \frac{\omega^2}{c^2} \vec{E} = 0. \quad (C.2)$$

A possible solution is a plane wave described by $e^{i\vec{k}\vec{r}}$. If the medium has no damping (i.e. it is transparent) the wave vector \vec{k} is real and can be written as:

$$k^2 = \varepsilon \mu \frac{\omega^2}{c^2} \quad (C.3)$$

This leads to the definition of the refractive index n and the wave velocity v in a medium:

$$n = \sqrt{\varepsilon \mu}, \quad v = \frac{c}{n} \quad (C.4)$$

Together with the result of last section, it follows immediately that:

At optical frequencies the refractive index is $n = \sqrt{\varepsilon}$ (in a homogeneous medium without damping)

\vec{E} and \vec{H} in a medium with damping

In a medium with damping \vec{k} becomes a complex value

$$\vec{k} = \vec{k}' + i\vec{k}'' \quad (C.5)$$

where \vec{k}' and \vec{k}'' are real vectors. The plane normal to \vec{k}' is the plane of constant phase, the plane of constant amplitudes lies normal to \vec{k}'' (the direction of damping of the wave).

Direct consequence of a complex \vec{k} is a complex refractive index $n_c = n + i\xi$, where n is the refractive index and ξ the absorption coefficient (latter describes the damping of the wave in the medium). From this (and $\mu = 1$) derives a complex dielectrical tensor $\varepsilon = \varepsilon' + i\varepsilon'' = n_c^2 = (n^2 - \xi^2) + i2n\xi$.

At optical frequencies $\epsilon = \epsilon' + i\epsilon''$, $n_c = n + i\xi$ (in a homogeneous medium with damping)

Consequences of a complex permittivity

The permittivity tensor can be written as a matrix. For solids with cubic or higher symmetry and a magnetization along the material \vec{z} -axis, it has the form:

$$\epsilon = \begin{pmatrix} \epsilon_{xx} & \epsilon_{xy} & 0 \\ -\epsilon_{xy} & \epsilon_{xx} & 0 \\ 0 & 0 & \epsilon_{zz} \end{pmatrix}_{cart} = \begin{pmatrix} \epsilon_{xx} + i\epsilon_{xy} & 0 & 0 \\ 0 & \epsilon_{xx} - i\epsilon_{xy} & 0 \\ 0 & 0 & \epsilon_{zz} \end{pmatrix}_{circ} \quad (C.6)$$

where the components ϵ_{ik} are all complex. It can be shown that this holds also for an arbitrary direction between \vec{M} and \vec{z} [Be64]¹.

It is now immediately visible that in circular coordinates the refractive index has two different values

$$n_c = \sqrt{\epsilon_{xx} \pm i\epsilon_{xy}} \quad (C.7)$$

belonging to left and right circularly polarized light. As in an isotropic (or cubic) medium the off-diagonal elements of the permittivity tensor vary linearly with magnetization [LL74], the generation of magneto-optical effects is now easy to show:

- **Change of the Kerr ellipticity ϵ :** The Kerr ellipticity ϵ is defined as $\frac{r_l - r_r}{r_l + r_r}$, where $r_{l,r}$ is the reflected amplitude of left and right circularly polarized light. The reflected wave can be described in terms of the incident wave by

$$E_{refl} = \frac{1 - n_c}{1 + n_c} \cdot E_{in} \quad (C.8)$$

As n_c has two different values the amplitude of the reflected left and right circularly polarized light will differ. This generates the observed change in ellipticity as is illustrated in figure C.1 b.

- **Change of the Kerr angle θ :** Different refractive indices means that the velocity of right polarized light in the medium is different from that of left polarized light. While the light propagates in the medium the phase difference between left and right polarized light will continuously increase. The Kerr angle being defined as $1/2 \cdot (\phi_l - \phi_r)$ this change will have an immediate impact (see also figure C.1 c).

The permittivity finally can be calculated from the measured Kerr angles and ellipticities by the formula:

$$\theta - i\epsilon = \frac{\epsilon_{ik}}{\sqrt{\epsilon_{ii}(\epsilon_{ii} - 1)}} \quad (C.9)$$

¹The authors use σ_{ik} instead of ϵ_{ik} . As these two quantities are linked by $\epsilon_{ij} = \delta_{ij} - i\sigma_{ij}4\pi/\omega$ the argument still holds.

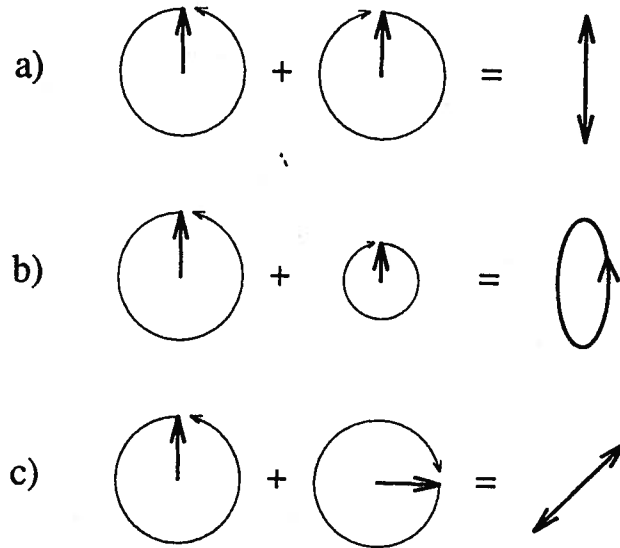


Figure C.1:

C.2 Microscopic description

At first sight one would expect the Kerr effect to be caused by an interaction of the H-field of the incident wave with the electron spin. But as was shown in the macroscopic approach the Kerr effect depends only on the permittivity of the material. The generator of the Kerr effect therefore must be an interaction of the E-field with the electron orbital motion.

An incident photon upon absorption will excite an atomic electron. The decay of the excited state will generally happen by electric dipole radiation as other channels are strongly suppressed. The selection rules important in this context are:

- $\Delta l = \pm 1$: the emitted photon has a momentum of $1 \hbar$
- $\Delta S = 0$: decays with spin flips are suppressed
- $\Delta m_j = 0, \pm 1$: determines the kind of emitted light, 0 corresponds to linearly, ± 1 to right and left circularly polarized light.

Relating these quantum mechanical quantities to solid state properties has been done by [Be64]. The complex part of the cross term conductivity tensor (and by consequence the refractive index related to it by Maxwell's field equation $(n_{r,l} + i\xi_{r,l})^2 = 1 + i(4\pi\sigma_{r,l}/\omega)$) can be expressed by a difference of transition matrices:

$$\sigma''_{xy}(\uparrow, \downarrow) \sim \sum_{i,f} (|\langle f(\uparrow, \downarrow) | \pi^- | i(\uparrow, \downarrow) \rangle|^2 - |\langle f(\uparrow, \downarrow) | \pi^+ | i(\uparrow, \downarrow) \rangle|^2) \cdot \delta(\omega_{if}(\uparrow, \downarrow) - \omega) \quad (\text{C.10})$$

π^\pm is the momentum operator including spin-orbit contribution.

Appendix C. Theoretical explanation of the Kerr effect

In a non-magnetized solid the energy emitted by a dipole transition is in first order dominated by the change from $|i\rangle$ with $l=x$ to $|f\rangle$ with $l=x-1$. Corrections due to exchange coupling and fine structure can be neglected in this context. Thus the two matrices cancel each other.

On the other hand when the solid is in a magnetic field the degeneracy of m_j is lifted by the Zeeman-Effect, $j-1$ sublevels appear. The frequency of a photon created at a transition with $m_j = +1$ is now different from a photon with $m_j = -1$. As the Zeeman effect goes linearly with B , the difference in photon frequency between spin up and spin down transitions increases also with magnetization. The intensity of the emitted dipole-radiation is now linked to its frequency by [Fr90]:

$$I(\omega)d\omega \sim \omega^3 d\omega \quad (\text{C.11})$$

Thus the existence of an energy difference in spin up and spin down transitions generates via the frequency-intensity relationship the observed change in Kerr ellipticity ϵ .

The change in Kerr angle is linked to the wave's travelling through matter and not to the way how it was generated. It is due to a different polarizability of the iron atom in the lattice for s- and p-waves.

A few concluding remarks. In the above discussion only the imaginary part of the conductivity tensor was mentioned. It can be shown that the real part σ'_{xy} is a function of σ''_{xy} . Thus knowledge of the latter is sufficient. In a solid there are no sharp energy levels but broad bands. This is no restriction to the qualitative nature of the result.

Appendix D

Suppliers

- **Laser diode:** Toshiba TOLD9140
- **Laser diode driver, laser collimator:** Seastar Optics Inc., Sidney, Canada, Fax (604) 655'34'35
- **All mountings, iris, lens:** OWIS GmbH, 7813 Staufen, Germany, Fax (07633) 8'27'27
- **Photo-elastic modulator:** Hinds Instruments Inc., Hillsboro OR, USA, Fax (503) 640'86'95
- **Wedge:** Melles Griot, Irvine CA, USA, Fax (714) 261'75'89
- **Diffuser:** Oriel Corporation, Stratford CT, USA, Fax (203) 378'24'57
- **Photodiode:** EG & G Optoelectronics, modell number C30808
- **Preamplifier:** Electronics workshop, Institute of physics, Basel, CH, plan number SP745
- **Lock-in amplifier:** EG & G, PARC 5210, Princeton NJ, USA, Fax (609) 883'72'59

Bibliography

- [Al86] R. Allenspach et al., *Phys Rev Lett* 56 9 (86) 953
- [Az88] R.M.A. Azzam and N.M. Bashara, *Ellipsometry and polarized light*, North-Holland physics publishing, 1988
- [Be64] H.S. Bennett and E.A. Stern, *Phys Rev* 137 2A (64) A448
- [Co75] P.S. Cooper, *PhD Thesis*, Yale University, 1975 and *A polarized electron target for Møller scattering*, Yale University, 1974
- [Da68] H. Danan, A. Herr and A.J.P. Meyer, *J Appl Phys* 39 2 (68) 669
- [Fo57] G.W. Ford and C.J. Mullin, *Phys Rev* 108 (57) 477
- [Fr87] A.J. Freemann et al., *J Appl Phys* 61 (87) 3356
- [Fr90] H. Friedrich, *Theoretische Atomphysik*, p. 105, Springer-Lehrbuch
- [Ha72] *Handbook of physics and chemistry*, p. 5-145, Table 5f-2
- [He28] W. Heisenberg, *Z Physik* 49 (28) 619
- [Hu67] R.P. Hunt, *J Appl Phys* 38 (67) 1652
- [Le92] L.G. Levchuk, *preprint SLAC Lib. KFTI 93-32*
- [Li85] Lindner, Brauer, Lehmann, *Taschenbuch der Elektrotechnik und Elektronik*, Verlag Harry Deutsch
- [LL74] L.D. Landau and E.M. Lifschitz, *Electrodynamics of continua*
- [Ma88] D. Mauri, *Phys Rev Lett* 61 9 (88) 758
- [Mo80] A.H. Morrish, *The physical principles of magnetism*, Robert E. Krieger Publishing Company, Huntington NY, 1980
- [OCLi] Calculated with the code EPC written by O'Connell and J. Lightbody
- [Ol68] H.A. Olsen, *Springer tracts in modern physics*, 1968

BIBLIOGRAPHY

- [Öz89] M. N. Özisik, *Boundary value problems of heat conduction*, Dover publications, 1989
- [Pi82] D.T. Pierce et al., *Phys Rev B* 26 5 (82) 2566
- [PP90] Particle properties data booklet, American Institute of physics, Berkeley and CERN
- [Po89] D.H. Potterveld, *PhD Thesis*, Caltech, 1989
- [Re69] R.A. Reck and D.L. Fry, *Phys Rev* 184 (69) 492
- [Ro63] C.C. Robinson, *J Opt Soc America* 53 (63) 681
- [Sc62] G.G. Scott, *Rev Mod Phys* 34 1 (62) 102
- [Sc67] D.M. Schwartz, *Phys Rev* 162 (67) 1306
- [Sc91] M.R. Scheinfein, *Phys Rev B* 43 4 (91) 3395
- [Wa86] B. Wagner, *PhD Thesis*, Mainz University, 1986; Equation [3.3] must be multiplied with m .
- [Wo86] P. Wolniansky et al., *J Appl Phys* 60 (86) 346

Curriculum vitae

Am 22. Februar 1963 wurde ich, Stephan Georg Robinson, geboren als Sohn von Christa und Derek Robinson. Von 1970 bis 1976 besuchte ich die Primarschule und von 1976 bis 1978 die Sekundarschule in Küsnacht ZH. 1978 trat ich in das Gymnasium Hottingen ZH über, welches ich im Herbst 1982 mit der Matura Typus E beendete. Im November 1983 begann ich an der Universität Basel das Studium der Experimentalphysik mit den Nebenfächern Mathematik und Astronomie. Im April 1989 folgte der Studienabschluss mit dem Diplom.

Seither arbeitete ich unter der Leitung von Prof. Dr. I. Sick an verschiedenen Streuexperimenten mit Hadronen am Injektorzyklotron des Paul-Scherrer-Institutes. Als Assistent war ich anfänglich im Anfänger-Praktikum tätig. Danach arbeitete ich für die 'Koordinationskommission für Universitätsfragen der Universität Basel'.

Meine Ausbildung in den Fächern Experimentalphysik, Theoretische Physik, Mathematik und Astronomie verdanke ich folgenden Dozentinnen und Dozenten:

K. Alder, G. Backenstoss, C. Bandle, E. Baumgartner, J. Fünfschilling, H.-J. Güntherodt, H. Huber, H. Kraft, P. Oelhafen, G.R. Plattner, H. Rudin, I. Sick, U. Steinlin, G. Tamman, L. Tauscher, D. Trautmann, C. Trefzger, R. Wagner, I. Zschokke.